Precision spectroscopy and comprehensive analysis of perturbations in the A $^1\Pi(v = 0)$ state of $^{13}C^{18}O$

Hakalla, R.; Trivikram, T. M.; Heays, A. N.; Salumbides, E. J.; de Oliveira, N.; Field, R. W.; Ubachs, W.

published in
Molecular Physics
2019

DOI (link to publisher)
10.1080/00268976.2018.1495848

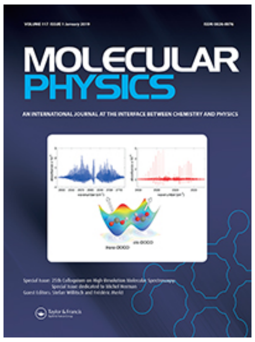

Taylor & Francis
Taylor & Francis Group

Molecular Physics

An International Journal at the Interface Between Chemistry and Physics

ISSN: 0026-8976 (Print) 1362-3028 (Online) Journal homepage: https://www.tandfonline.com/loi/tmph20

Precision spectroscopy and comprehensive analysis of perturbations in the $A^1\Pi(v = 0)$ state of $^{13}C^{18}O$

R. Hakalla, T. M. Trivikram, A. N. Heays, E. J. Salumbides, N. de Oliveira, R. W. Field & W. Ubachs

MOLECULAR PHYSICS
2019, VOL. 117, NO. 1, 79–96
https://doi.org/10.1080/00268976.2018.1495848

RESEARCH ARTICLE

Precision spectroscopy and comprehensive analysis of perturbations in the $A^1\Pi(v=0)$ state of $^{13}C^{18}O$

R. Hakalla[a], T. M. Trivikram[b], A. N. Heays[c,d], E. J. Salumbides[b], N. de Oliveira[e], R. W. Field[f] and W. Ubachs[b]

[a]Materials Spectroscopy Laboratory, Faculty of Mathematics and Natural Science, University of Rzeszów, RZ, Poland; [b]Department of Physics and Astronomy and LaserLaB, Vrije Universiteit, Amsterdam, Netherlands; [c]LERMA, Observatoire de Paris, PSL Research University, CNRS, Sorbonne Universités, Paris, France; [d]School of Earth and Space Exploration, Arizona State University, Tempe, AZ, USA; [e]Synchrotron SOLEIL, St. Aubin, France; [f]Department of Chemistry, Massachusetts Institute of Technology, Cambridge, MA, USA

ABSTRACT

We have reinvestigated the $A^1\Pi(v=0)$ level of $^{13}C^{18}O$ using new high-resolution spectra obtained via multi-photon laser excitation as well as with synchrotron-based Fourier-transform absorption spectroscopy of the $A^1\Pi - X^1\Sigma^+(0,0)$, $e^3\Sigma^- - X^1\Sigma^+(1,0)$, $d^3\Delta - X^1\Sigma^+(4,0)$, $a'^3\Sigma^+ - X^1\Sigma^+(9,0)$, and $a^3\Pi - X^1\Sigma^+(11,0)$ bands. In addition, Fourier-transform emission spectroscopy in the visible range is performed on the $B^1\Sigma^+ - A^1\Pi(0,0)$ band. Spectra of the $B^1\Sigma^+ - X^1\Sigma^+(0,0)$ band are measured in order to tie information from the latter emission data to the level structure of $A^1\Pi(v=0)$. The high pressures in the absorption cell at the synchrotron and the high temperatures in the emission discharge permitted monitoring of high rotational quantum levels in $A^1\Pi(v=0)$ up to $J=43$. All information, in total over 900 spectral lines, was included in an effective Hamiltonian analysis of the $A^1\Pi(v=0,J)$ levels that are directly perturbed by the $e\,^3\Sigma^-(v=1)$, $d^3\Delta(v=4)$, $a'^3\Sigma^+(v=9)$, $D\,^1\Delta(v=0)$, $I\,^1\Sigma^-(v=0,1)$ close-lying levels and the $e\,^3\Sigma^-(v=0,2)$, $d^3\Delta(v=3,5)$, $a'^3\Sigma^+(v=8,10)$ remote levels, as well being indirectly influenced by the $a^3\Pi(v=10,11)$ state. The influence of 9 further perturber levels and their interactions was investigated and are not significant for reproducing the present experimental data. This analysis leads to a much improved description in terms of molecular constants and interaction parameters, compared to previous studies of the same energy region for other CO isotopologues.

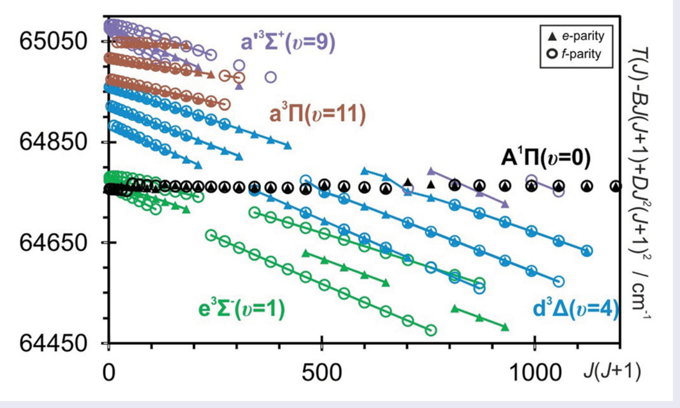

ARTICLE HISTORY
Received 9 April 2018
Accepted 11 June 2018

KEYWORDS
Laser spectroscopy; Fourier-transform spectroscopy; carbon monoxide; isotopologues; deperturbation analysis

1. Introduction

The spectroscopy of the carbon monoxide molecule is of major importance in view of its being the second most abundant molecule in the Universe. Its dipole moment is a decisive ingredient in the cooling process of interstellar clouds *en route* to star formation. The probing of CO under a variety of conditions is crucial to an understanding of the physics and chemistry of the interstellar medium [1], of protoplanetary disks [2], of exoplanetary atmospheres [3], of galactic structure at large redshifts [4] and it may turn out to be a probe of temporal variation of fundamental constants [5,6]. In view of

CONTACT R. Hakalla hakalla@ur.edu.pl Materials Spectroscopy Laboratory, Faculty of Mathematics and Natural Science, University of Rzeszów, Pigonia 1 Street, 35-959 Rzeszów, Poland

Supplemental data for this article can be accessed here. https://doi.org/10.1080/00268976.2018.1495848

saturation and shielding effects of the strongest transitions, the use and investigation of lower-abundance isotope-substituted species is of relevance, in particular where photo-dissociation becomes strongly isotope dependent [7,8], in some cases connected to subtle effects of perturbations [9,10].

The CO molecule is a prototypical system for investigating perturbations in the spectra of diatomic molecules, as is known since the studies by Field on the $A^1\Pi$ state [11,12]. In recent years, our team has been involved in detailed re-investigations of perturbations in the $A^1\Pi$ state of CO, exploiting a combination of various precision spectroscopic techniques, where the lowest v' 0 vibrational level was chosen as a main target. One of the aims of pursuing a precision study of the $A^1\Pi$ state was the derivation of sensitivity coefficients for probing a possible variation of fundamental constants based on the $A^1\Pi - X^1\Sigma^+$ system of CO [13]. Thereafter, precision studies of the $A^1\Pi - X^1\Sigma^+(0,0)$ bands and the perturbing states were performed for $^{12}C^{16}O$ [14], for $^{13}C^{16}O$ [15], for $^{13}C^{17}O$ [16] and for $^{12}C^{18}O$ [17]. Here, we extend these studies on the $^{13}C^{18}O$ isotopologue using laser-based excitation and vacuum ultraviolet-Fourier-transform (FT-VUV) absorption spectroscopy as well as visible Fourier-transform (FT-VIS) emission spectroscopy to observe and assign the perturbations in the $A^1\Pi(v=0)$ state. In the other isotopologues, perturbing effects of the $a'^3\Sigma^+(v=9)$, $d^3\Delta(v=4)$, $e\,^3\Sigma^-(v=1)$, $I\,^1\Sigma^-(v=0,\,1)$ and $D\,^1\Delta(v=0)$ levels were found and these will also be investigated here. Also, perturbations by levels of the $a^3\Pi$ state will be addressed. Therefore, in addition to low-pressure FT-VUV studies performed, focusing on the $A^1\Pi - X^1\Sigma^+$ excitation, high$^{13}C^{18}O$ pressures were used to observe the weak absorption of the $a^3\Pi - X^1\Sigma^+$, $d^3\Delta - X^1\Sigma^+$, $a'^3\Sigma^+ - X^1\Sigma^+$ and $e^3\Sigma^- - X^1\Sigma^+$ systems. These measurements provide additional and accurate information about the perturbing effects on the $A^1\Pi$ state. In particular, the intensity borrowing effects between the singlet and triplet systems tightly constrain the values of the perturbation parameters.

Although the $A^1\Pi - X^1\Sigma^+$ system of CO has been investigated in many studies over the decades, the information on the $^{13}C^{18}O$ isotopologue is scarce. Haridass and co-workers have performed detailed studies of $A^1\Pi(v=0)$ by VUV emission, revealing perturbation effects from the $a'^3\Sigma^+(v=10)$ and $d^3\Delta(v=5)$ levels [18,19]. Emission studies of the Ångström ($B^1\Sigma^+$—$A^1\Pi$) bands of $^{13}C^{18}O$ [20,21] provided further information on the $A^1\Pi(v=0)$ level, and the study of the Herzberg ($C^1\Sigma^+ - A^1\Pi$) systems [22,23] also provided detailed information on the interaction with the $e\,^3\Sigma^-(v=1)$ level. The $A^1\Pi - X^1\Sigma^+$ system was reinvestigated recently with the FT-VUV spectrometer at the SOLEIL synchrotron [24], focusing on the determination of term values and line strength parameters. In that study, the existence of two additional dipole-allowed singlet systems, denoted as $1^1\Sigma^+ - X^1\Sigma^+$ and $1^1\Pi - X^1\Sigma^+$, was hypothesised. Information on the perturbing triplet states in $^{13}C^{18}O$ has not yet been reported, except for the study of the $a^3\Pi(v=0)$ state [25].

The present study entails a high-precision re-analysis of the level structure of the $A^1\Pi(v=0)$ state of $^{13}C^{18}O$, following the rotational manifold up to the rotational quantum number $J=43$. This results in a much improved description in terms of molecular constants and interaction parameters, and a comparison is made with previous studies.

2. Experimental procedures

As in previous studies on the $^{13}C^{16}O$ [15] and $^{12}C^{18}O$ [17] isotopologues, three distinct experimental techniques are employed to assess the rotational level structure of the $A^1\Pi(v=0)$ manifold. The most accurate $A^1\Pi - X^1\Sigma^+(0,0)$ line frequencies were derived from Doppler-free measurements using a narrowband laser source, consisting of a pulsed-dye-amplifier (PDA) injection seeded by the continuous-wave output of a ring-dye laser [26]. A $2+1'$ resonance enhanced multi-photon ionisation laser scheme was used for two-photon excitation of the low J rotational levels of the $A^1\Pi - X^1\Sigma^+(0,0)$ band, followed by ionisation by a second UV laser pulse at 203 nm, as described in Niu et al. [27]. Mass-dependent detection of CO isotopologues was achieved in a time-of-flight mass spectrometer. An isotopically enriched $^{13}C^{18}O$ gas sample was used for the experiment (Sigma Aldrich, 99% atom ^{13}C and 95% atom ^{18}O). Absolute frequencies were determined by simultaneous recording of saturated I_2 resonances [28] and markers from a stabilised etalon. Frequency chirp effects in the PDA laser were measured and corrected for off-line, but their uncertainties nevertheless contribute decisively to the uncertainty budget of the laser experiments. The transition frequencies were measured for a range of laser intensities in the focal region to assess the AC-Stark effect; extrapolation to zero intensity resulted in the true transition frequencies. The overall accuracy of the transition frequencies falls between 0.002 and 0.003 cm^{-1}. The laser-based experiments were carried out at LaserLaB Amsterdam.

Visible emission data were recorded from a hollow-cathode discharge lamp. It was initially filled with a mixture of helium and acetylene $^{13}C_2D_2$ (Cambridge Isotopes, 99.98% of ^{13}C) at a pressure of approximately 10 mbar. A DC electric current was passed through the mixture for about 150 hours. The process, similar to that described by Hakalla et al. [16,29], resulted in the deposition of a small amount of ^{13}C inside the cathode. Next, the lamp was evacuated and filled with an enriched sample of $^{18}O_2$ gas (Sigma Aldrich, 98.1%). The electrodes were operated at 950 V and 80 mA DC with a static gas pressure of 3 mbar. The higher temperature of the $^{13}C^{18}O$ plasma formed at the centre of the cathode, up to 1000 K, allowed for observations of rotational transitions with J up to 41; a higher value than in our previous experiments [30,31]. The physical line-broadening increased by only 0.02 cm^{-1} relative to that reported in [32,33], where the temperatures of plasmas were about 650 K. The final molecular gas composition used to obtain the spectrum was $^{13}C^{18}O : {}^{12}C^{18}O = 1 : 0.1$. The spectral emission was analysed by a 1.7 m FT spectrometer used under vacuum conditions. Operation of the setup and calibration procedures were explained in recent reports on the setup installed at Rzeszów University [15–17]. Spectra were accumulated over 128 scans with a spectral resolution of 0.018 cm^{-1}. The accuracy on the transition frequencies amounts to 0.003–0.03 cm^{-1}.

The setup involving the FT-VUV spectrometer at the SOLEIL synchrotron [34,35] was employed to obtain absorption spectra of $^{13}C^{18}O$ under three regimes. First, spectra of the $A^1\Pi - X^1\Sigma^+(0,0)$ band were measured under conditions of low gas density in a quasi-static flow through a windowless cell, with column densities in the range 10^{14} to 2×10^{15} cm^{-2}, as in previous studies [14,24,36,37]. This provides spectroscopic information on J-levels up to about 20. Second, further $A^1\Pi - X^1\Sigma^+(0,0)$ spectra were recorded at high gas pressures (up to about 80 mbar) in a closed cell of 9 cm length and sealed by magnesium-fluoride windows [37]. This enabled probing lines with J up to 43 and the detection of many more lines of the perturbing $e^3\Sigma^- - X^1\Sigma^+$, $d^3\Delta - X^1\Sigma^+$, $a'^3\Sigma^+ - X^1\Sigma^+$ and $a^3\Pi - X^1\Sigma^+$ forbidden band systems. An approximate column density of 2×10^{19} cm^{-2} was achieved in this case. The full width half maximum self-broadening of lines in the $A^1\Pi - X^1\Sigma^+(20,0)$ and (21, 0) bands of $^{12}C^{16}O$ is measured to be $(2.3 \pm 0.5) \times 10^{-4}$ cm^{-1} mbar^{-1} [38], leading to a maximum broadening in our case of 0.02 cm^{-1} that is not detectable due to significantly greater broadening arising from the Doppler effect and finite instrumental resolution.

Finally, the $B^1\Sigma^+ - X^1\Sigma^+(0,0)$ band was recorded in a heated windowless cell, attaining a rotational temperature of ~ 1000 K in a setup similar to that of Niu et al. [39]. Transition frequencies deduced from FT-VUV spectra have accuracies estimated to fall in the range 0.02–0.05 cm^{-1}, depending on the specific conditions under which the spectra were recorded and the blendedness, weakness or saturation of individual absorption lines. The lower uncertainty limit generally applies to the low-density room-temperature spectra, while greater uncertainties are associated with higher temperature and pressure spectra.

3. Results

In the following the results of all individual studies are presented.

3.1. Results from laser-based study

Laser-based $2 + 1'$ REMPI spectra were recorded for nine two-photon transitions of the $A^1\Pi - X^1\Sigma^+(0,0)$ band. Figure 1 displays a spectrum of the $Q(1)$ line. All

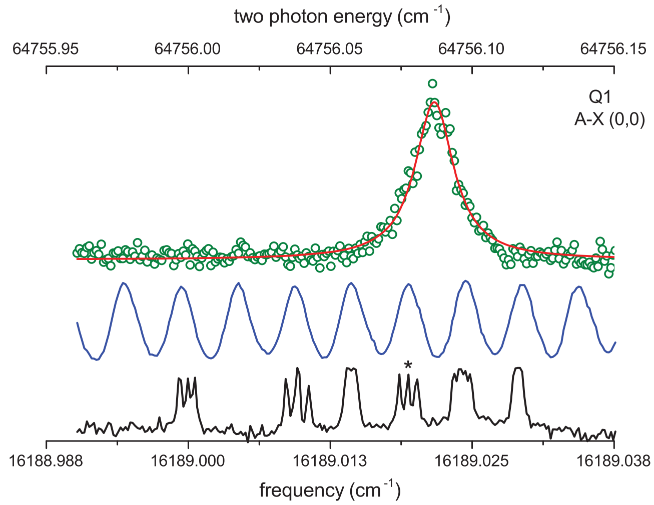

Figure 1. The $A^1\Pi - X^1\Sigma^+$ (0, 0) $Q(1)$ transition measured by $2 + 1'$ REMPI (open points and upper curve fitted to them). The middle line and lower line show etalon markers from a stabilised Fabry–Perot interferometer and the saturated iodine spectrum used for frequency interpolation and calibration, respectively. The asterisk indicates the a13 hyperfine component of the B-X (10, 3) $R(87)$ iodine line at 16,189.019 45 cm^{-1} [28] that was used for an absolute calibration.

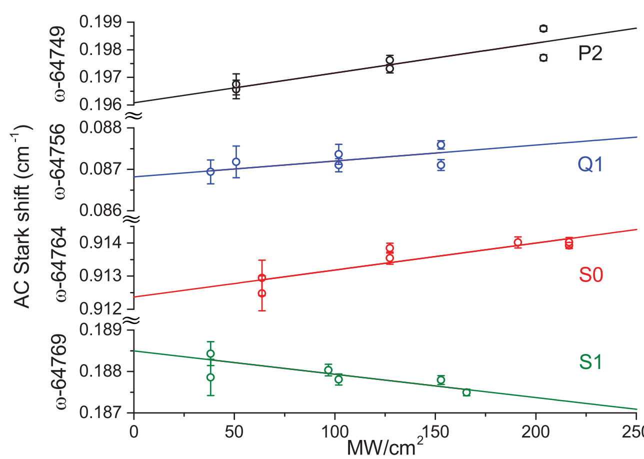

Figure 2. AC-Stark-plots for four $A^1\Pi - X^1\Sigma^+(0,0)$ two-photon transitions.

line measurements were performed as a function of laser power density in the focal region, similarly to the previous study of $^{12}C^{18}O$ [17]. Figure 2 shows the AC-Stark extrapolation curves for four selected lines. The transition frequencies were derived from extrapolation to zero intensity levels and are listed in Table 1.

Table 1. Results from the two-photon Doppler-free laser experiment. Measured $A^1\Pi - X^1\Sigma^+$ (0, 0) transition frequencies, ν_{obs}, and AC-Stark slope coefficients, C_{AC}, for four selected lines.

Line	ν_{obs} [a]	C_{AC} [b]
$P(2)$	64 749.1956 (20)	0.32
$P(3)$	64 744.3124 (30)	
$Q(1)$	64 756.0869 (30)	0.11
$Q(2)$	64 754.4352 (20)	
$R(1)$	64 761.7759 (30)	
$R(2)$	64 763.1306 (20)	
$S(0)$	64 764.9124 (30)	0.24
$S(1)$	64 769.1883 (30)	−0.16
$S(2)$	64 771.9897 (30)	

[a] Units of cm^{-1} and 1σ uncertainties given in parentheses in units of the least-significant digit.
[b] Units of $MHz/(MW/cm^2)$.

Interestingly, the sign of the AC-Stark slope is negative for the $S(1)$ two-photon transition, while the slope for the other transitions is positive (see Figure 2). From a reanalysis of the data reported in [15] it is found that the sign of the AC-Stark slope for the $S(1)$ line in $^{13}C^{16}O$ is also negative, while all other lines exhibit a positive AC-Stark slope. In contrast, for all lines in $^{12}C^{18}O$ [17] a positive AC-Stark slope is found. This phenomenon is connected to the molecular level structure at the three-photon excitation level in the molecule and can be studied in further detail by performing two-colour ionisation experiments [40].

3.2. Results from FT-VIS study

Here, we present the results of the FT emission study of the $^{13}C^{18}O$ $B^1\Sigma^+ - A^1\Pi(0, 0)$ band and the perturbing lines in the wavelength range $\lambda = 438$–452 nm, with a measured spectrum shown in Figure 3 (an electronic form of the Figure 3 source spectrum is given in the Supplementary Material). This range

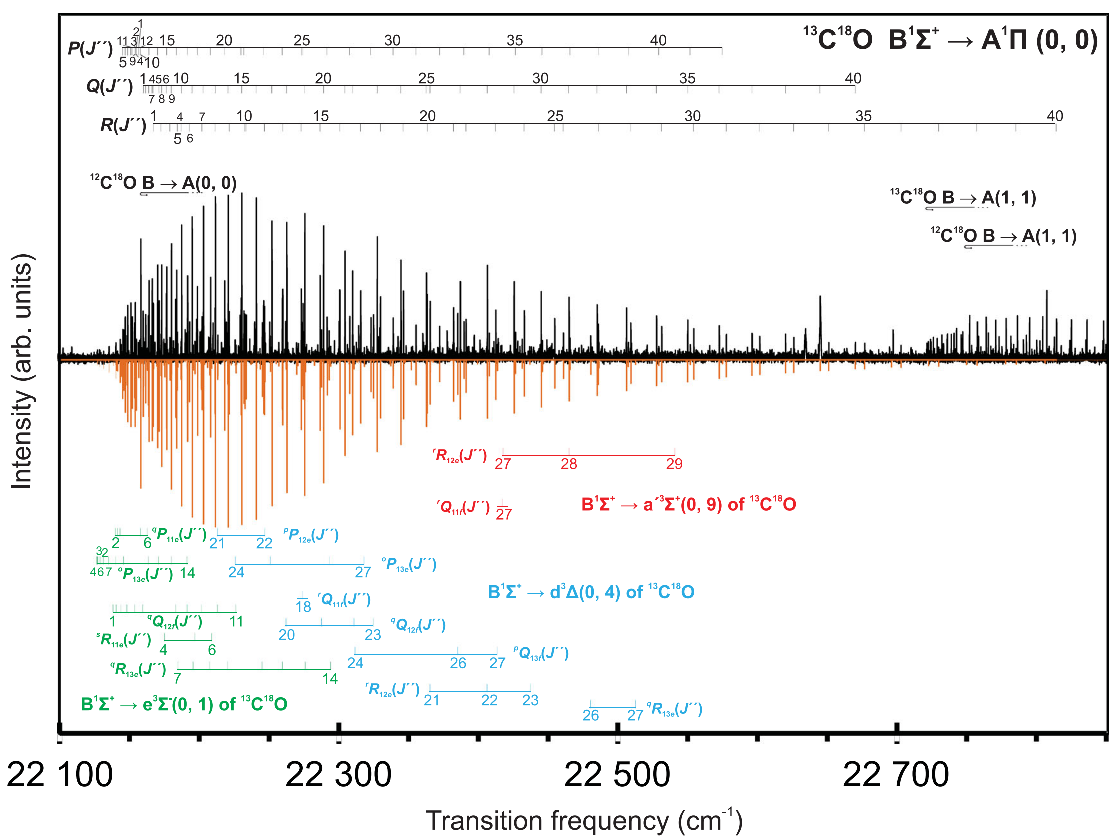

Figure 3. VIS high-resolution photo-emission spectra recorded by the FT spectroscopy technique. Observed $^{13}C^{18}O$ rovibronic bands are indicated. The upper trace presents an experimental spectrum, whereas the lower one shows a simulated spectrum of the $^{13}C^{18}O$ $B^1\Sigma^+ - A^1\Pi$ (0, 0) band and lines terminating on states perturbing $A^1\Pi(v = 0)$. The simulation is obtained using the PGOPHER software [42].

Table 2. Transition frequencies of the $^{13}C^{18}O$ $B^1\Sigma^+ - A^1\Pi$ (0,0) band obtained from the FT-VIS experiment.[a]

J''	$R(J'')$	$o-c$	$Q(J'')$	$o-c$	$P(J'')$	$o-c$
1	22 168.40 (2) [bw]	0.01	22 161.219 (6) [b]	−0.005	22 157.80 (2) [bw]	0.02
2	22 173.685 (8) [bw]	0.003	22 162.736 (6) [b]	0.025	22 155.992 (6) [bw]	0.007
3	22 180.077 (6) [b]	0.005	22 164.996 (3) [b]	0.009	22 155.295 (5)	−0.003
4	22 187.995 (7) [b]	0.019	22 168.127 (2)	0.007	22 156.125 (6) [bw]	0.001
5	22 185.288 (5) [b]	0.003	22 172.235 (2)	0.007	22 146.351 (4) [b]	−0.008
6	22 194.047 (4)	−0.001	22 177.491 (2)	−0.007	22 148.048 (3)	0.002
7	22 202.956 (3)	−0.002	22 167.340 (2)	−0.003	22 149.885 (3)	0.002
8	22 212.326 (3) [b]	−0.002	22 174.118 (2)	−0.001	22 152.182 (2)	−0.001
9	22 222.401 (3)	−0.004	22 181.087 (1)	−0.002	22 155.188 (2)	−0.004
10	22 233.471 (3)	−0.004	22 188.309 (1)	−0.002	22 159.191 (1) [b]	−0.006
11	22 234.468 (3)	0.010	22 195.890 (1)	−0.002	22 153.110 (4) [b]	−0.008
12	22 247.593 (3)	0.007	22 203.925 (1)	−0.001	22 159.191 (1) [b]	0.006
13	22 260.615 (2)	0.006	22 212.475 (1)	−0.002	22 165.159 (2)	0.007
14	22 273.776 (2)	0.005	22 221.591 (1)	−0.002	22 171.269 (2) [b]	0.009
15	22 287.312 (2) [b]	0.005	22 231.313 (1)	−0.002	22 177.753 (2)	0.006
16	22 301.344 (2) *	−0.037	22 241.693 (1)	−0.002	22 184.781 (2)	0.005
17	22 316.275 (2)	0.001	22 252.908 (1) *	−0.045	22 192.633 (2) *	0.004
18	22 330.357 (3)	0.008	22 263.422 (1)	−0.005	22 199.627 (2) *	−0.041
19	22 346.758 (2)	0.007	22 276.290 (1)	0.002	22 209.038 (2)	−0.001
20	22 363.791 (2)	0.003	22 289.781 (1)	−0.001	22 219.056 (2)	0.006
21	22 382.617 (3) [b]	0.002	22 305.061 (1)	−0.005	22 230.859 (2)	0.003
22	22 391.537 (3)	0.004	22 310.448 (2)	0.004	22 232.767 (3)	0.007
23	22 412.671 (3)	0.008	22 328.087 (1)	0.001	22 246.892 (3)	0.011
24	22 433.056 (3)	0.009	22 344.976 (2)	0.004	22 260.259 (3) [b]	−0.004
25	22 454.772 (3) [b]	0.010	22 363.200 (2)	0.002	22 274.991 (3) [b]	0.009
26	22 460.981 (5)	−0.010	22 365.815 (2) [b]	−0.009	22 274.202 (4) [b]	−0.020
27	22 486.036 (3)	−0.004	22 387.367 (2)	−0.001	22 292.283 (3)	−0.004
28	22 509.103 (4)	−0.003	22 406.747 (2)	0.001	22 308.379 (3)	0.001
29	22 531.185 (4) [b]	−0.009	22 425.817 (2)	0.004	22 323.505 (3)	0.006
30	22 554.083 (4) [b]	−0.007	22 445.157 (2)	0.003	22 339.437 (3)	0.001
31	22 577.379 (6) [b]	0.013	22 465.003 (2)	−0.004	22 355.751 (4) [b]	−0.011
32	22 601.178 (7) [b]	0.015	22 485.099 (2)	−0.013	22 372.614 (4) [b]	−0.004
33	22 625.517 (7) [b]	−0.012	22 506.080 (3)	0.001	22 390.021 (3) [b]	−0.027
34	22 650.496 (8) *	0.004	22 527.581 (3)	−0.011	22 408.071 (5) [b]	−0.015
35	22 676.090 (8) *[b]	−0.044	22 549.742 (3) *[b]	−0.011	22 426.779 (6) *[b]	−0.033
36	22 702.125 (8) [b]	0.068	22 572.317 (4) *[b]	0.048	22 445.881 (6) *[b]	0.054
37	22 728.91 (2) [bw]	0.03	22 595.689 (6) [b]	0.028	22 465.779 (6) [b]	0.018
38	22 756.299 (9) [bw]	0.007	22 619.635 (5) [b]	0.007	22 486.292 (7) [b]	0.013
39	22 784.31 (1) [bw]	0.01	22 644.228 (2) [b]	0.012	22 507.427 (7) [b]	0.005
40	22 812.93 (3) [bw]	0.03	22 669.458 (7) [bw]	0.027	22 529.184 (9) [bs]	−0.014
41					22 551.57 (3) [bbs]	−0.04
42					22 574.62 (3) [bbs]	−0.05

Notes: The number in parentheses indicates the uncertainty of expected line position given by the empirical relation in Equation (1). Lines marked with 'b' and/or 'w' are blended and/or weak. For lines marked by an asterisk (*) a very weak perturbation in the $B^1\Sigma^+(v=0)$ Rydberg state was found. The instrumental resolution was 0.018 cm^{-1}. The estimated absolute calibration uncertainty (1σ) was 0.003 cm^{-1}. The column with $o-c$ displays the deviations between observed values and values calculated by the fitting routine.[a] In units of cm^{-1}.

covers an interval where perturber-state lines of $B^1\Sigma^+ - e^3\Sigma^-(0,1)$, $B^1\Sigma^+ - d^3\Delta(0,4)$ and $B^1\Sigma^+ - a'^3\Sigma^+(0,9)$ bands can be identified. Source contamination by $^{12}C^{18}O$ $B^1\Sigma^+ - A^1\Pi(0,0)$, $^{13}C^{18}O$ $B^1\Sigma^+ - A^1\Pi(1,1)$ and $^{12}C^{18}O$ $B^1\Sigma^+ - A^1\Pi(1,1)$ bands was taken into consideration during the analysis. Measured transition frequencies of $^{13}C^{18}O$ $B^1\Sigma^+ - A^1\Pi(0,0)$ are listed in Table 2, while the lines connecting the $B^1\Sigma^+(v=0)$ upper state to perturber levels are listed in Table 3. Line positions were measured by fitting Voigt lineshape functions to the experimental lines. Line position uncertainties were evaluated using an empirical relation similar to that given by Brault [41]:

$$\Delta\sigma = \frac{f}{\sqrt{N}} \frac{\text{FWHM}}{\sqrt{\text{SNR}}}, \qquad (1)$$

where f is a constant of the order of unity that is lineshape dependent, FWHM is the full width at half maximum of the line, N is the true number of statistically independent points in a linewidth (taking into account the zero filling factor commonly used to interpolate FT spectra), and SNR is the signal-to-noise ratio.

3.3. FT-VUV $A \leftarrow X$ system

A combination of small and large column density spectra showing $^{13}C^{18}O$ $A^1\Pi - X^1\Sigma^+(0,0)$ measured with the FT-VUV is shown in Figure 4 (an electronic form of the Figure 4 source spectrum is provided in the Supplementary Material). The location of rotational transitions attributed to $A^1\Pi - X^1\Sigma^+(0,0)$ are presented

Table 3. Spin-forbidden lines appearing in the FT-VIS emission spectrum of $^{13}C^{18}O$.[a]

J''	$^{S}R_{11ee}$	$o-c$	$^{r}Q_{11ef}$	$o-c$	$^{q}P_{11ee}$	$o-c$
			$B^1\Sigma^+ - e^3\Sigma^-(0,1)$			
2					22 141.04 (2) [bw]	−0.02
3					22 142.58 (2) [bw]	0.02
4	22 176.344 (8) [b]	−0.011			22 144.496 (6) [b]	−0.008
5	22 197.886 (6) [b]	−0.004			22 158.968 (6)	0.005
6	22 209.90 (2) [b]	−0.02			22 163.92 (2) [bw]	0.01
			$B^1\Sigma^+ - d^3\Delta(0,4)$			
18			22 270.377 (8)	0.006		
19						
			$B^1\Sigma^+ - a'^3\Sigma^+(0,9)$			
27			22 418.12 (3) [bw]	0.02		
	$^{r}R_{12ee}$	$o-c$	$^{q}Q_{12ef}$	$o-c$	$^{p}P_{12ee}$	$o-c$
			$B^1\Sigma^+ - e^3\Sigma^-(0,1)$			
1			22 139.49 (2) [bw]	0.04		
2			22 141.72 (2) [bw]	−0.02		
3			22 145.115 (9) [b]	0.010		
4			22 149.509 (7) [b]	0.008		
5			22 154.822 (4) [b]	0.017		
6			22 160.830 (2)	−0.004		
7			22 184.176 (2)	0.007		
8			22 192.455 (3)	−0.003		
9			22 202.439 (4) [b]	−0.001		
10			22 214.06 (2) [bw]	0.01		
11			22 227.202 (8) [bw]	−0.002		
			$B^1\Sigma^+ - d^3\Delta(0,4)$			
20			22 263.02 (2) [b]	−0.04		
21	22 365.93 (1) [b]	0.02	22 288.291 (4) [b]	−0.009	22 214.153 (4) [b]	−0.006
22	22 406.548 (5)	−0.009	22 325.445 (3)	−0.008	22 247.777 (4)	−0.007
23	22 437.07 (2) [b]	−0.01	22 352.439 (9) [b]	−0.003		
			$B^1\Sigma^+ - a'^3\Sigma^+(0,9)$			
27	22 459.58 (2) [b]	−0.01				
28	22 501.46 (7) [b]	−0.01				
29	22 545.39 (2) [bw]	0.02				
	$^{q}R_{13ee}$	$o-c$	$^{p}Q_{13ef}$	$o-c$	$^{o}P_{13ee}$	$o-c$
			$B^1\Sigma^+ - e^3\Sigma^-(0,1)$			
2					22 130.75 (2) [bw]	−0.02
3					22 128.752 (4) [bw]	0.022
4					22 127.921 (7) [bw]	0.019
5					22 128.281 (9) [bw]	0.002
6					22 129.867 (4) [bw]	0.016
7	22 185.663 (7) [b]	−0.006			22 132.60 (2) [bw]	0.01
8	22 196.597 (8) [b]	−0.006			22 136.43 (1) [bw]	−0.03
9	22 208.55 (1) [b]	−0.01			22 141.345 (9) [b]	0.005
10	22 221.308 (4) [b]	0.005			22 147.028 (4) [b]	0.004
11	22 245.970 (4) [b]	−0.001			22 164.628 (2)	−0.003
12	22 260.39 (2) [b]	0.04			22 171.949 (6) [b]	0.002
13	22 276.74 (2) [b]	0.04			22 181.231 (6) [b]	−0.013
14	22 294.78 (2) [b]	−0.03			22 192.28 (2) [b]	−0.01
			$B^1\Sigma^+ - d^3\Delta(0,4)$			
24			22 311.53 (2) [b]	−0.02	22 226.91 (2) [b]	0.01
25					22 251.703 (9) [b]	−0.008
26	22 480.494 (6) [b]	−0.013	22 385.490 (5) [b]	−0.004	22 293.740 (5) [b]	0.002
27	22 512.52 (2)	−0.02	22 413.852 (9) [b]	0.015	22 318.775 (9) [b]	−0.013

Notes: The number in parentheses indicates the uncertainty of expected line position given by the empirical relation (1). Lines marked with 'w' and/or 'b' are weak and/or blended. The instrumental resolution was 0.018 cm^{-1}. The estimated absolute calibration uncertainty (1σ) was 0.003 cm^{-1}. The column with $o-c$ displays the deviations between observed values and values calculated by the fitting routine. The branch-label subscripts *e* and *f* indicate the upper state/lower state symmetry and superscripts *o,p,q,r* and *s* denote change in the total angular momentum excluding spin.

[a] All transition frequencies are in cm^{-1}.

in Table 4, while the transition frequencies of four forbidden bands, $e^3\Sigma^- - X^1\Sigma^+(1,0)$, $d^3\Delta - X^1\Sigma^+(4,0)$, $a'^3\Sigma^+ - X^1\Sigma^+(9,0)$ and $a^3\Pi - X^1\Sigma^+(11,0)$, are indicated in this figure and listed in Tables 5– 8.

A detailed spectrum covering 100 cm^{-1} of the high-column density spectrum is plotted in Figure 5 and demonstrates the detection of some of these weak transitions. The assignment of the highly congested high-density spectrum was greatly facilitated by simultaneously refining the level-interaction model described in Section 4. Additionally, the purified $^{13}C^{18}O$ sample gas contained minor contamination from the $^{13}C^{16}O$,

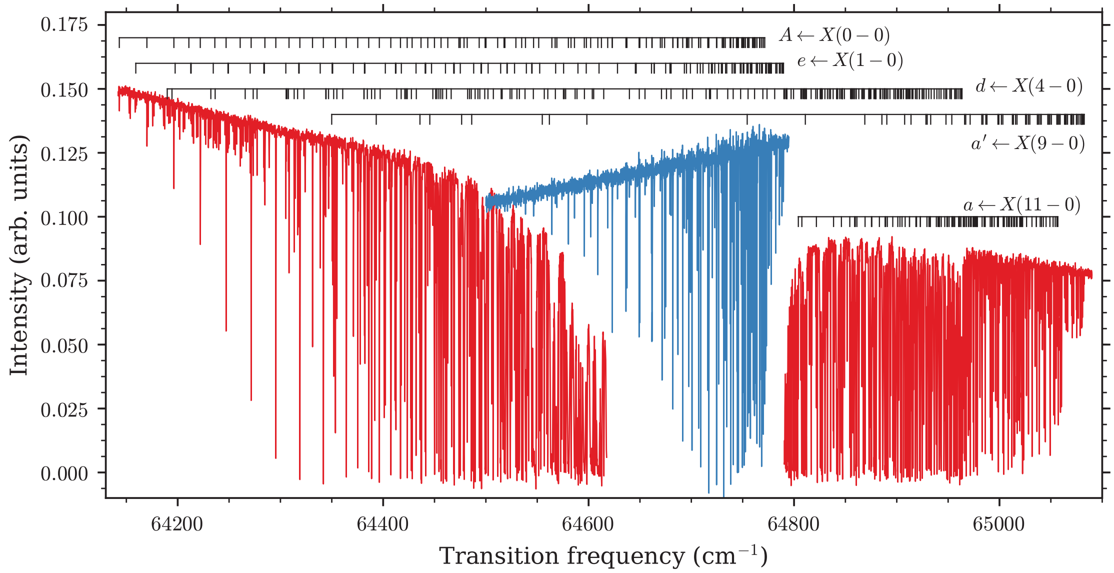

Figure 4. VUV photoabsorption spectra recorded with small and large column densities (center trace and edge traces, respectively). Observed lines attributed to $^{13}C^{18}O$ electronic-vibrational bands are indicated. There is significant absorption due to other CO isotopologues. A variable background intensity slope due to the synchrotron-radiation wavelength dependence is evident.

$^{13}C^{17}O$ and $^{12}C^{18}O$ isotopologues, which had to be distinguished from forbidden $^{13}C^{18}O$ transitions. The estimated ratio amounts about $^{13}C^{18}O$: $^{13}C^{16}O$: $^{13}C^{17}O$: $^{12}C^{18}O = 1 : 0.04 : 0.003 : 0.0002$. Of the many hundreds of lines observed in the spectra, only some eight lines of non-negligible intensity remain unassigned.

Several assumptions were made while analysing these spectra in order to accurately measure the frequencies and absorption depths of blended and weak lines. The term-value combination differences for *P*- and *R*-branch lines connected to a common upper rotational level were fixed by reference to accurately-known $^{13}C^{18}O$ ground state term values [43] and the ratio of $P(J''-1)/R(J''+1)$ line strengths of all bands was assumed proportional to the corresponding Hönl-London factors for a $^1\Pi - {}^1\Sigma^+$ transition. This provided an excellent fit to the measured absorption lineshapes and is justified given that the sole source of intensity in this spectral region is the $A\,^1\Pi{-}X\,^1\Sigma^+$ transition moment, which will maintain its $^1\Pi - {}^1\Sigma^+$ character even when redistributed into nominally forbidden bands. Additionally, absorption intensities attributed to $a'^3\Sigma^+ - X^1\Sigma^+$ (9, 0) were not found to be strongly *J*-dependent once the ground state thermal-population and Hönl-London factors were factored out. Then, this band was modelled assuming a quadratic $J(J+1)$ dependence for its band absorption oscillator strengths. Normally distributed 1σ-uncertainties for all fitting parameters are estimated from a Hessian matrix computed by the least-squares fitting routine with respect to the fit residual. These uncertainties should be accurate if all assumptions described above are reasonable and the model parameters are not highly correlated. Testing this scheme with an ensemble of synthetic experimental data finds good agreement between estimated uncertainties and statistics of the ensemble. A minimum uncertainty of 0.05 cm^{-1} was assumed for frequencies determined from overlapped and saturated lines. All measured transition frequencies are subject to a common systematic uncertainty associated with the overall frequency calibration. A calibration of the SOLEIL low-pressure spectra was made with respect to the laser-based measurements of Section 3.1. The low-*J* lines of $^{13}C^{18}O$, which are accurately calibrated from the laser spectra (with correction for Λ-doubling) are all saturated in the high-pressure spectrum and the contaminating lines of $^{13}C^{16}O$ were instead used for its calibration, with reference to our previous study of this isotopologue [36]. The systematic frequency uncertainty is estimated to be 0.01 cm^{-1}.

To conclude, we find no need to assign lines to additional electronic transitions, beyond the ones known to exist in this energy range of CO. All lines that were postulated to belong to the *P*- and *R*-transitions in a $1^1\Sigma^+$ – $X^1\Sigma^+$ band system and to *Q*-branch transitions in a $2^1\Pi$ - $X^1\Sigma^+$ band system in a previous study [24] could be assigned to $A^1\Pi - X^1\Sigma^+(0,0)$ lines and perturber lines of $^{13}C^{18}O$ as found in the present paper.

Table 4. Measured VUV absorption frequencies[a] of $A \leftarrow X(0,0)$.

J''	P_{11ee}	Q_{11fe}	R_{11ee}
0	–	–	64 759.580(1)
1	–	64 756.184(1)	64 761.421(1)
2	64 749.101(1)	64 754.789(1)	64 762.2024(9)
3	64 743.958(1)	64 752.652(1)	64 761.511(1)
4	64 737.7545(9)	64 749.709(1)	64 771.4740(9)
5	64 730.079(1)	64 745.832(1)	64 770.019(1)
6	64 733.0599(9)	64 740.845(1)	64 768.460(1)
7	64 724.623(1)	64 751.331(1)	64 766.489(1)
8	64 716.085(1)	64 744.926(1)	64 763.855(1)
9	64 707.136(1)	64 738.376(2)	64 760.268(1)
10	64 697.527(1)	64 731.619(1)	64 766.806(1)
11	64 686.966(1)	64 724.529(3)	64 761.245(2)
12	64 686.533(1)	64 717.08(4)	64 755.838(1)
13	64 674.003(2)	64 709.122(1)	64 750.333(2)
14	64 661.631(1)	64 700.653(2)	64 744.493(2)
15	64 649.165(2)	64 691.629(2)	64 738.160(3)
16	64 636.367(2)	64 681.990(2)	64 731.048(2)
17	64 623.078(3)	64 671.514(2)	64 724.791(4)
18	64 609.016(2)	64 661.872(3)	64 716.247(4)
19	64 595.813(4)	64 649.880(3)	64 707.115(7)
20	64 580.327(4)	64 637.314(4)	64 696.222(7)
21	64 564.258(7)	64 623.004(7)	64 695.29(1)
22	64 546.433(7)	64 618.606(9)	64 682.16(2)
23	64 538.57(1)	64 602.018(8)	64 669.84(2)
24	64 518.52(2)	64 586.24(1)	64 656.21(3)
25	64 499.28(5)	64 569.13(3)	–
26	64 478.74(5)	–	–
27	64 473.75(5)	–	–
28	64 449.96(5)	64 529.24(5)	64 612.50(5)
29	64 428.20(5)	64 511.49(5)	64 597.86(5)
30	64 407.46(5)	64 493.50(5)	64 582.88(5)
31	64 385.95(5)	64 475.05(5)	64 567.42(5)
32	64 364.10(5)	64 456.36(5)	64 551.43(5)
33	64 341.77(5)	64 436.86(5)	64 534.866(5)
34	64 318.93(5)	64 416.86(5)	64 517.679(5)
35	64 295.519(5)	64 396.28(5)	64 500.120(5)
36	64 271.495(5)	64 375.27(5)	64 481.810(5)
37	64 247.107(5)	64 353.537(5)	64 462.935(5)
38	64 221.977(5)	64 331.243(5)	64 443.461(6)
39	64 196.290(5)	64 308.360(5)	64 423.39(5)
40	64 170.014(6)	64 284.886(9)	–
41	64 143.15(5)	64 260.81(2)	–
42	–	64 236.15(3)	–
43	–	64 210.88(5)	–

[a] In units of cm^{-1} and with 1σ statistical uncertainties given in parentheses in units of the least-significant digit. The total uncertainty is the sum in quadrature of these and a 0.01 cm^{-1} systematic uncertainty.

3.4. FT-VUV $B \leftarrow X$ system

A spectrum of $B^1\Sigma^+ - X^1\Sigma^+(0,0)$ was recorded with the FT-VUV setup at SOLEIL while $^{13}C^{18}O$ flowed through a windowless cell heated to approximately 1000 K [39]. The column density for this measurement was approximately 7×10^{15} cm^{-2} and overlapping $B^1\Sigma^+ - X^1\Sigma^+(0,0)$ absorption from the $^{12}C^{16}O$, $^{13}C^{16}O$, $^{13}C^{17}O$ and $^{12}C^{18}O$ isotopologues, as well as the $B^1\Sigma^+ - X^1\Sigma^+(1,0)$ band of $^{13}C^{18}O$, had to be included in the analysis of this spectrum, with observed rotational levels up to $J = 51$.

Measured $B^1\Sigma^+ - X^1\Sigma^+(0,0)$ transition frequencies and term values are listed in Table 9 and Supplemantary Table 17, respectively. The purpose of measuring this band is twofold. First, transition frequencies from the $B^1\Sigma^+ - A^1\Pi(0,0)$ FT-VIS spectrum can be converted to absolute $A(\nu\,0)$-state term values when combined with the $B^1\Sigma^+ - X^1\Sigma^+(0,0)$ data and known ground state levels. Second, there occur weak (less than 0.05 cm^{-1}) perturbations in the $B^1\Sigma^+ - X^1\Sigma^+(0,0)$ spectrum leading to the $B(v = 0)$ term energy shifts shown in Figure 6 at $J = 17$, and between 30 and 35. Care was taken that these were not misinterpreted as shifts of $A^1\Pi(\nu = 0)$ levels while analysing the $B^1\Sigma^+ - A^1\Pi(0,0)$ spectrum. The frequency calibration of this spectrum was made with respect to atomic lines contaminating the spectrum and adopted NIST frequencies for Xe (lines at 83 889.97, 85 440.02 and 90 032.18 cm^{-1}), Kr (85 846.71 cm^{-1}) and O (86 794.15 cm^{-1}). This calibration is estimated to impart a systematic uncertainty of 0.01 cm^{-1} to the measured line frequencies of this band.

4. Deperturbation analysis

It is well known that the $A^1\Pi(v = 0)$ level is extensively perturbed in all CO isotopologues, with the occurrence of multiple rotational level crossings with other electronic-vibrational states and smaller effects due to more remote non-crossing levels [11,14,16]. The long-lived $e\,^3\Sigma^-(v = 1)$, $d^3\Delta(v = 4)$, $a'^3\Sigma^+(v = 9)$ levels are primarily responsible for the perturbations through their homogeneous spin–orbit interaction with $A^1\Pi(\nu = 0)$, with magnitudes parameterised by η. Additionally, the shorter-lived $D\,^1\Delta(v = 0)$ and $I\,^1\Sigma^-(v = 0,1)$ states heterogeneously perturb $A^1\Pi(=0)$ through L-uncoupling interactions, parameterised by ξ. Rostas and co-workers [44–46] showed that interactions with multiple $A^1\Pi$ vibrational levels contribute to the intensity borrowing of forbidden bands. Therefore, the present deperturbation analysis includes some additional levels that affect $A^1\Pi(\nu = 0)$ relatively weakly or indirectly, that is $e\,^3\Sigma^-(v = 0,2)$, $d^3\Delta(\nu = 3,5)$, $a'^3\Sigma^+(\nu = 8,10)$ and $a^3\Pi(\nu = 10,11)$. They were not considered in our work on other CO isotopologues but are included now in the light of a larger experimental data set. Figure 7 shows plots of calculated rovibronic level energies against $J(J+1)$ for $A^1\Pi(\nu = 0)$ and its nearest neighbours, showing the crossing points where local perturbations may occur, whereas Figure 8 presents experimental reduced terms obtained in this work.

For the mutual interactions between $a^3\Pi$ and the other triplet states under consideration, there are two perturbation mechanisms in operation: spin–orbit and those that arise from the $\mathbf{B}(\mathbf{R}^2)$ term of the rotational Hamiltonian. Writing the latter as $\mathbf{R} = \mathbf{J} - \mathbf{L} - \mathbf{S}$ we get $\mathbf{J}\cdot\mathbf{L}$, $\mathbf{J}\cdot\mathbf{S}$ and $\mathbf{L}\cdot\mathbf{S}$ terms, respectively L-uncoupling, S-uncoupling and spin-electronic coupling. The $\Delta\Omega = 0$ spin-electronic matrix element is explicitly related to

Table 5. Measured VUV absorption frequencies[a] of $d \leftarrow X(4,0)$.

J''	P_{11ee}	P_{21ee}	P_{31ee}	Q_{11fe}	Q_{21fe}	Q_{31fe}	R_{11ee}	R_{21ee}	R_{31ee}
0	–	–	–	–	–	–	–	–	64 962.130(5)
1	–	–	–	–	–	64 958.641(5)	–	64 926.495(5)	64 963.385(5)
2	–	–	64 951.651(5)	–	64 919.52(2)	64 956.409(5)	–	64 926.261(5)	64 963.523(5)
3	–	64 909.032(5)	64 945.921(5)	64 879.39(5)	64 915.776(5)	64 953.079(7)	64 887.87(5)	64 924.794(5)	64 962.564(5)
4	–	64 901.813(5)	64 939.075(5)	64 873.86(3)	64 910.826(5)	64 948.63(1)	64 884.49(2)	64 922.082(5)	64 960.502(5)
5	64 856.44(5)	64 893.362(5)	64 931.132(5)	64 866.96(1)	64 904.624(5)	64 943.088(5)	64 879.614(8)	64 918.134(5)	64 957.330(5)
6	64 846.08(2)	64 883.668(5)	64 922.088(5)	64 858.703(9)	64 897.183(5)	64 936.434(5)	64 873.491(5)	64 912.943(5)	64 953.044(9)
7	64 834.219(8)	64 872.738(5)	64 911.935(5)	64 849.052(5)	64 888.53(5)	64 928.670(5)	64 866.001(5)	64 906.520(5)	64 947.675(5)
8	64 821.116(5)	64 860.568(5)	64 900.670(9)	64 838.071(5)	64 878.584(5)	64 919.799(9)	64 857.172(5)	64 898.847(5)	64 941.162(5)
9	64 806.648(5)	64 847.167(5)	64 888.322(5)	64 825.753(9)	64 867.429(5)	64 909.794(5)	64 847.00(5)	64 889.939(5)	64 933.513(5)
10	64 790.843(5)	64 832.518(5)	64 874.834(5)	64 812.095(5)	64 855.030(5)	64 898.633(7)	64 835.512(5)	64 879.795(5)	64 924.719(5)
11	64 773.70(5)	64 816.637(5)	64 860.211(5)	64 797.119(5)	64 841.400(5)	64 886.368(5)	64 822.702(5)	64 868.403(5)	64 914.756(5)
12	64 755.238(5)	64 799.522(5)	64 844.446(5)	–	64 826.54(1)	64 872.918(5)	64 808.583(5)	64 855.780(5)	64 903.619(5)
13	64 735.460(5)	64 781.162(5)	64 827.515(5)	–	64 810.42(3)	64 858.291(5)	64 793.11(5)	64 841.924(5)	64 891.300(5)
14	64 714.376(5)	64 761.574(5)	64 809.413(5)	–	–	64 842.481(5)	–	64 826.82(1)	64 877.787(5)
15	64 691.94(5)	64 740.756(5)	64 790.132(5)	–	–	64 825.46(1)	–	64 810.51(2)	64 863.078(5)
16	–	64 718.69(1)	64 769.660(5)	–	–	64 807.293(5)	–	64 792.99(5)	64 847.158(7)
17	–	64 695.43(2)	64 747.997(5)	–	–	–	64 717.70(2)	–	64 830.066(5)
18	–	64 670.96(5)	64 725.126(7)	64 654.91(2)	–	–	–	–	64 811.732(6)
19	64 588.72(2)	–	64 701.088(5)	–	–	–	–	–	64 792.208(6)
20	64 560.294(5)	–	64 675.813(6)	–	–	–	–	–	–
21	64 530.256(5)	–	64 649.351(6)	64 575.52(2)	64 639.74(2)	–	–	64 680.23(4)	–
22	64 498.90(3)	–	–	–	64 603.58(2)	–	64 595.950(6)	–	–
23	64 466.226(5)	64 523.541(7)	–	64 515.858(5)	64 577.667(7)	–	64 567.667(9)	–	–
24	64 432.312(6)	64 494.124(5)	–	64 484.118(5)	–	–	64 538.11(2)	64 604.955(5)	–
25	64 397.114(9)	64 461.670(5)	64 532.644(5)	64 451.103(7)	–	–	64 507.29(2)	64 576.257(5)	–
26	64 360.65(2)	64 427.491(5)	64 502.030(5)	–	64 485.796(5)	–	–	64 546.224(5)	64 614.732(5)
27	64 322.92(2)	64 391.889(5)	64 454.221(5)	64 381.27(3)	64 452.312(5)	–	–	64 514.887(5)	64 586.878(5)
28	–	64 354.959(5)	64 423.467(5)	64 344.48(3)	64 417.534(5)	64 489.539(5)	–	64 482.271(6)	64 556.877(5)
29	–	64 316.732(5)	64 388.723(5)	64 306.41(5)	64 381.463(6)	64 456.08(1)	–	64 448.38(1)	64 525.287(5)
30	–	64 277.231(6)	64 351.837(5)	–	64 344.138(9)	64 421.047(5)	–	64 413.23(3)	64 492.275(6)
31	–	64 236.46(1)	64 313.371(5)	–	64 305.56(2)	64 384.606(5)	–	–	64 457.94(2)
32	–	64 194.44(3)	64 273.489(6)	–	64 265.71(3)	64 346.84(1)	–	–	64 422.31(2)
33	–	–	64 232.29(2)	–	–	64 307.78(2)	–	–	–
34	–	–	64 189.81(2)	–	–	–	–	–	–

[a] In units of cm^{-1} and with 1σ statistical uncertainties given in parentheses in units of the least-significant digit. The total uncertainty is the sum in quadrature of these and a 0.01 cm^{-1} systematic uncertainty.

the $\Delta\Omega = 1$ L-uncoupling matrix element, because they both consist of an experimentally determined $\langle\Pi|\mathbf{L}^+|\Sigma\rangle$ factor, multiplied by an explicitly known matrix element factor depending only on the spin [12]. This means that the perturbation terms derived from the rotational operator have $\Delta\Omega = 0$ and $\Delta\Omega = 1$ matrix elements, the values of which are explicitly locked together. The $a^3\Pi \sim (D\,^1\Delta,\ I\,^1\Sigma^-)$ and $a'^3\Sigma^+ \sim e\,^3\Sigma^-$ interactions arise from spin–orbit interactions. Finally, the $d^3\Delta \sim (a'^3\Sigma^+,\ e\,^3\Sigma^-)$ perturbations come from spin–spin interactions represented by the ϵ perturbation parameter. Effects of the direct $A^1\Pi(v{=}0) \sim a^3\Pi(v{=}10{,}11)$ spin–orbit interactions are too weak to be deduced from the data set. This might be ascribed to very small vibrational overlap integrals $\langle v_{A(0)}|v_{a(10)}\rangle = 1.4 \times 10^{-4}$ and $\langle v_{A(0)}|v_{a(11)}\rangle = -1.6 \times 10^{-3}$. Some of the indirect $A^1\Pi \sim (e\,^3\Sigma^-,\ d^3\Delta,\ a'^3\Sigma^+) \sim a^3\Pi$ perturbations significantly shift the observed $A^1\Pi$ levels and are analysed in detail. All of the close-lying levels taken into consideration intersect $A(v = 0)$ in their zero-order approximation except for $I(v = 0, 1)$, $D(v = 0)$, $e(v = 2)$, $d(v = 5)$ and $a'(v = 10)$, which nevertheless have a noticeable direct influence on $A(v = 0)$.

In order to find deperturbed molecular constants for $A^1\Pi(v{=}0)$, we use the PGOPHER software [42] to model this level and all neighbouring perturber levels with an effective Hamiltonian matrix with diagonal elements composed of deperturbed constants describing each electronic-vibrational level and off-diagonal elements given by the various possible perturbation parameters arising from the spin–orbit, L-uncoupling, spin-electronic and spin–spin operators. The manifold of levels surrounding $A(v = 0)$ is combined with unperturbed models of the $X(v = 0)$ and $B(v = 0)$ levels to simulate transition frequencies for the experimentally observed bands: $A^1\Pi - X^1\Sigma^+(0,0)$, $B^1\Sigma^+ - A^1\Pi(0,0)$, $B^1\Sigma^+ - e^3\Sigma^-(0,1)$, $B^1\Sigma^+ - d^3\Delta(0,4)$, $B^1\Sigma^+ - a'^3\Sigma^+(0,9)$, $B^1\Sigma^+ - X^1\Sigma^+(0,0)$, $a^3\Pi - X^1\Sigma^+(11,0)$, $a'^3\Sigma^+ - X^1\Sigma^+(9,0)$, $d^3\Delta - X^1\Sigma^+(4,0)$ and $e^3\Sigma^- - X^1\Sigma^+(1,0)$. In total, 908 experimental frequencies from 10 bands of $^{13}C^{18}O$ were used to iteratively refine the free parameters of the effective Hamiltonian model until good general agreement was obtained.

Table 6. Measured VUV absorption frequencies[a] of e ← X(1, 0).

J''	P_{11ee}	P_{31ee}	Q_{21fe}	R_{11ee}	R_{31ee}
0	–	–	–	64 776.99(2)	64 783.37(1)
1	–	–	64 777.968(7)	64 776.347(7)	64 786.637(9)
2	64 766.51(2)	64 772.89(1)	64 775.773(4)	64 774.932(3)	64 788.766(8)
3	64 758.884(7)	64 769.173(9)	64 772.529(5)	64 773.138(2)	64 789.725(8)
4	64 750.484(3)	64 764.318(8)	64 768.333(4)	64 758.864(4)	64 789.548(9)
5	64 741.707(2)	64 758.293(8)	64 763.261(2)	64 754.149(4)	64 788.210(5)
6	64 720.450(4)	64 751.134(9)	64 757.511(2)	64 747.650(7)	64 785.746(4)
7	64 708.754(4)	64 742.814(5)	64 734.499(2)	64 739.66(2)	64 782.209(3)
8	64 695.275(7)	64 733.372(4)	64 726.583(2)	64 730.26(1)	64 777.693(3)
9	64 680.31(2)	64 722.856(3)	64 717.0(1)	64 719.62(3)	64 772.427(3)
10	64 663.94(1)	64 711.364(3)	64 705.864(4)	–	64 755.303(2)
11	64 646.32(3)	64 699.125(3)	64 693.238(7)	–	64 748.495(3)
12	–	64 675.030(2)	64 679.210(9)	–	64 739.748(8)
13	–	64 661.254(3)	64 663.83(7)	–	64 729.304(9)
14	–	64 645.541(8)	–	–	–
15	–	64 628.136(9)	–	–	–
16	64 539.422(5)	–	–	64 610.166(5)	–
17	64 514.39(1)	–	–	64 589.644(5)	–
18	64 488.135(5)	–	–	64 567.926(5)	–
19	64 460.666(5)	64 544.628(5)	–	64 544.987(5)	–
20	64 432.006(5)	64 520.54(3)	–	64 520.834(5)	–
21	64 402.130(5)	64 495.26(5)	64 495.717(5)	64 495.465(5)	64 597.716(5)
22	64 371.045(5)	64 468.744(5)	64 469.181(5)	64 468.888(7)	64 575.677(5)
23	64 338.749(5)	64 441.000(5)	64 441.423(5)	64 441.09(1)	64 552.405(5)
24	64 305.250(7)	64 412.039(5)	64 412.447(5)	64 412.08(2)	64 527.912(5)
25	64 270.54(1)	64 381.851(5)	64 382.257(5)	64 381.87(2)	64 502.191(8)
26	64 234.61(2)	64 350.449(5)	64 350.848(5)	64 350.47(3)	64 475.11(2)
27	64 197.50(2)	64 317.824(8)	64 318.234(8)	–	64 447.10(1)
28	64 159.20(3)	64 283.84(2)	64 284.40(1)	–	–
29	–	64 248.95(1)	64 249.34(2)	–	–
30	–	64 212.66(5)	64 213.09(4)	–	–

[a]In units of cm^{-1} and with 1σ statistical uncertainties given in parentheses in units of the least-significant digit. The total uncertainty is the sum in quadrature of these and a 0.01 cm^{-1} systematic uncertainty.

Table 7. Measured VUV absorption frequencies[a] of a ← X(11, 0).

J''	P_{11ee}	P_{21ee}	P_{31ee}	Q_{11fe}	Q_{21fe}	Q_{31fe}	R_{11ee}	R_{21ee}	R_{31ee}
0	–	–	–	–	–	–	64 976.03(2)	65 019.973(5)	–
1	–	–	–	–	65 016.477(5)	–	64 977.677(5)	65 021.675(5)	–
2	64 965.55(2)	65 009.495(5)	–	64 972.523(5)	65 014.692(5)	–	64 978.389(5)	65 022.467(5)	–
3	64 960.214(5)	65 004.211(5)	–	64 969.713(5)	65 012.030(5)	–	64 978.149(5)	65 022.403(5)	–
4	64 953.942(5)	64 998.019(5)	–	64 965.952(5)	65 008.503(5)	65 042.68(3)	64 976.955(5)	65 021.490(5)	–
5	64 946.717(5)	64 990.971(5)	–	64 961.220(5)	65 004.123(5)	65 039.63(1)	64 974.788(5)	65 019.741(5)	65 056.84(2)
6	64 938.541(5)	64 983.076(5)	–	64 955.517(5)	64 998.926(5)	65 035.88(1)	64 971.650(5)	65 017.176(5)	65 055.95(2)
7	64 929.393(5)	64 974.346(5)	65 011.45(2)	64 948.86(5)	64 992.905(5)	65 031.54(5)	64 967.527(5)	65 013.805(5)	65 054.28(1)
8	64 919.275(5)	64 964.801(5)	65 003.57(2)	64 941.16(5)	64 986.083(5)	65 026.48(2)	64 962.443(5)	65 009.636(5)	65 052.19(4)
9	64 908.175(5)	64 954.452(5)	64 994.92(1)	64 932.56(3)	64 978.49(1)	65 020.66(1)	64 956.407(5)	65 004.664(5)	65 049.09(3)
10	64 896.114(5)	64 943.307(5)	64 985.86(4)	64 922.981(5)	64 970.063(5)	–	64 949.416(5)	64 998.920(6)	65 045.36(1)
11	64 883.105(5)	64 931.362(5)	64 975.79(3)	64 912.48(1)	64 960.872(5)	65 006.97(1)	64 941.504(5)	64 992.371(5)	65 040.92(2)
12	64 869.144(5)	64 918.647(6)	64 965.09(1)	64 901.008(9)	64 950.926(6)	–	64 932.678(5)	64 985.042(6)	65 035.71(5)
13	64 854.263(5)	64 905.130(5)	64 953.68(2)	64 888.65(5)	64 940.138(5)	–	64 922.942(5)	64 976.887(9)	–
14	64 838.471(5)	64 890.836(6)	64 941.50(5)	64 875.386(7)	–	–	64 912.316(5)	64 967.73(2)	–
15	64 821.774(5)	64 875.719(9)	–	64 861.204(7)	–	–	–	–	–
16	64 804.190(5)	64 859.60(2)	–	64 846.127(5)	64 903.10(2)	–	–	–	–
17	–	–	–	–	64 889.21(2)	–	–	–	–
18	–	–	–	–	–	–	–	–	–
19	–	–	–	–	64 858.97(4)	–	–	–	–

[a]In units of cm^{-1} and with 1σ statistical uncertainties given in parentheses in units of the least-significant digit. The total uncertainty is the sum in quadrature of these and a 0.01 cm^{-1} systematic uncertainty.

Full details of our methodology were presented in previous works [14,47] and the Hamiltonian used in it is described by Western [53]. The explicit formulation of the effective Hamiltonian and matrix elements are contained in the Pgopher file, with a final version is provided in the Supplementary Material. Initial estimates for the parameter values governing excited states are adopted in analogy to other CO isotopologues, using the isotope-scaling constants deduced by Field et al. [11,12,48], Niu et al. [14,36], Le Floch et al. [51], Yamamoto and Saito

Table 8. Measured VUV absorption frequencies[a] of $a' \leftarrow X(9,0)$.

J''	P_{21ee}	Q_{11fe}	Q_{31fe}	R_{21ee}
0	–	–	–	65 079.97(1)
1	–	65 074.91(1)	65 082.50(2)	65 080.794(8)
2	65 069.49(1)	65 070.29(1)	65 081.82(1)	65 080.288(7)
3	65 063.331(8)	65 064.224(8)	65 079.88(1)	65 078.447(6)
4	65 055.840(7)	65 056.768(9)	65 076.660(9)	65 075.276(5)
5	65 047.015(6)	65 047.989(7)	65 072.105(9)	65 070.777(5)
6	65 036.862(5)	65 037.897(7)	65 066.253(8)	65 064.945(6)
7	65 025.381(5)	65 026.36(3)	65 059.066(8)	65 057.837(6)
8	65 012.570(6)	65 013.54(1)	65 050.552(8)	65 049.10(1)
9	64 998.484(6)	64 999.40(1)	65 040.710(9)	65 039.357(9)
10	64 982.77(1)	64 983.93(1)	65 029.550(8)	65 028.19(2)
11	64 966.055(9)	64 967.15(2)	65 017.06(1)	65 015.66(1)
12	64 947.92(2)	–	65 003.28(2)	65 001.88(1)
13	64 928.41(1)	–	64 987.80(1)	64 986.71(2)
14	64 907.68(1)	–	64 971.44(2)	–
15	64 885.55(2)	–	64 953.60(2)	–
16	–	–	–	64 933.03(5)
17	–	–	64 913.88(2)	–
18	64 811.00(5)	–	–	–
19	–	–	64 868.90(5)	–
26	–	64 554.926(7)	–	–
28	64 476.41(1)	–	–	64 598.320(5)
29	64 435.837(5)	–	–	64 561.84(2)
30	64 393.280(5)	–	–	–
31	64 349.92(2)	–	64 486.221(7)	–
32	–	–	64 445.434(7)	–

[a] In units of cm^{-1} and with 1σ statistical uncertainties given in parentheses in units of the least-significant digit. The total uncertainty is the sum in quadrature of these and a 0.01 cm^{-1} systematic uncertainty.

[52] and Kittrell and Garetz [50]. Ground state constants for $^{13}C^{18}O$ are taken from Coxon and Hajigeorgiou [43] and are kept fixed in all fitting procedures. Constants describing $B(v=0)$ were fit to its experimentally deduced term values. A computed correlation matrix of all model parameters is monitored during the fitting process to determine a minimal set of molecular constants necessary to model the experimental data. Some parameters, afflicted by a high degree of correlation with others but verified to be significant were held fixed to estimated values. They are calculated as described by Hakalla et al. [16,47]. The value of interactions involving the $a^3\Pi(v=10,11)$ levels are calculated using elements of an effective Hamiltonian matrix defined in Table IV of Field et al. [11] optimised by comparing them with the symmetrised matrix elements used in the current fit [42] as well as electronic perturbation matrix elements given in Table IV of Ref. [12]. In the final fit, 39 independent parameters were adjusted and their best-fit values are listed in Table 10. The root-mean-square error of modelled transition frequencies is then 0.02 cm^{-1}.

All the $a^3\Pi \sim d^3\Delta$ and $a^3\Pi \sim a'^3\Sigma^+$ interactions reported in Table 10 have η and ξ parameters with opposite sign. This is a consequence of the dominant electronic

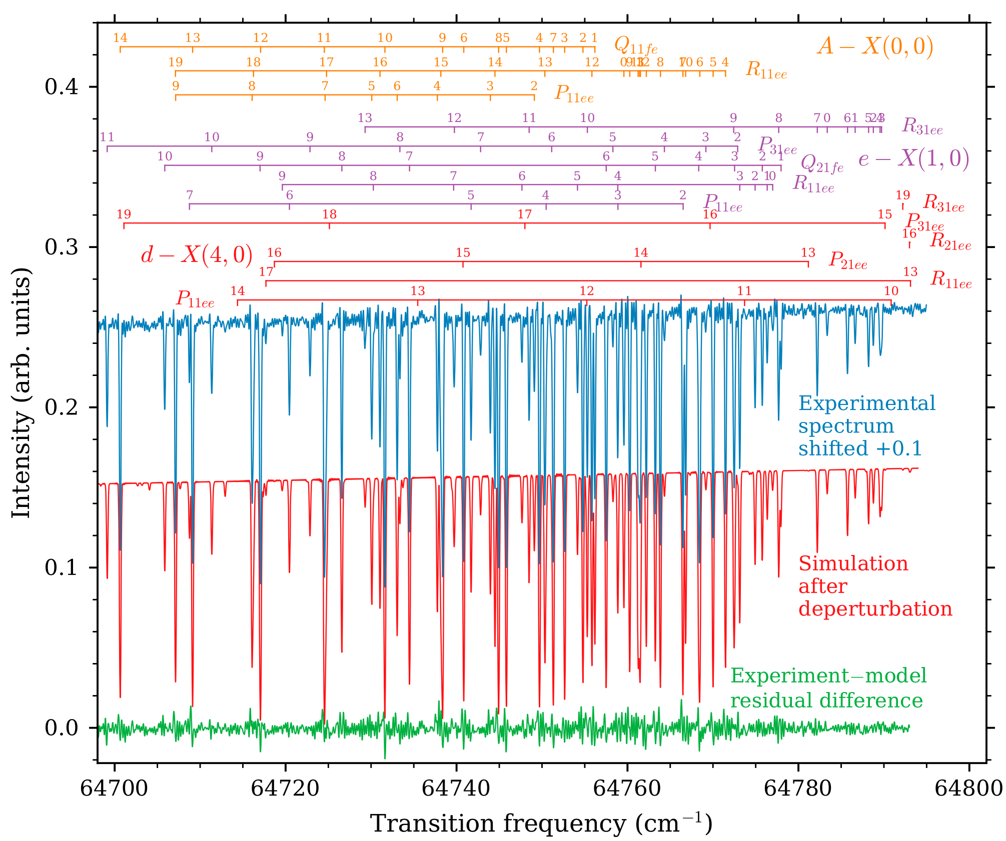

Figure 5. A detailed partial view of the experimental VUV photoabsorption spectra recorded with large column density, a simulated spectrum employing the effective Hamiltonian model, and their difference. The simulation incorporates several instrumental effects: an assumed column density, the sloping source intensity, instrumental and Doppler broadening.

Table 9. Measured FT-VUV absorption frequencies[a] of B← X(0, 0).

J''	P_{11ee}	R_{11ee}
0	–	86 920.896(1)
1	86 913.862(2)	86 924.483(1)
2	86 910.418(1)	86 928.1164(9)
3	86 907.020(1)	86 931.7944(8)
4	86 903.6685(9)	86 935.5212(8)
5	86 900.3628(8)	86 939.2919(7)
6	86 897.1071(8)	86 943.1082(7)
7	86 893.8966(7)	86 946.9702(7)
8	86 890.7332(7)	86 950.8773(7)
9	86 887.6174(7)	86 954.8299(7)
10	86 884.5487(7)	86 958.8257(8)
11	86 881.5279(7)	86 962.8701(8)
12	86 878.5527(8)	86 966.9544(8)
13	86 875.6290(8)	86 971.0857(8)
14	86 872.7481(8)	86 975.2595(9)
15	86 869.9176(8)	86 979.4751(9)
16	86 867.1331(9)	86 983.694(1)
17	86 864.3941(9)	86 988.035(1)
18	86 861.662(1)	86 992.390(1)
19	86 859.057(1)	86 996.776(1)
20	86 856.470(1)	87 001.205(1)
21	86 853.919(1)	87 005.677(1)
22	86 851.416(1)	87 010.189(1)
23	86 848.961(1)	87 014.744(2)
24	86 846.551(1)	87 019.336(2)
25	86 844.190(2)	87 023.973(2)
26	86 841.872(2)	87 028.651(2)
27	86 839.606(2)	87 033.359(2)
28	86 837.386(2)	87 038.106(2)
29	86 835.204(2)	87 042.899(2)
30	86 833.067(2)	87 047.714(2)
31	86 830.982(2)	87 052.576(2)
32	86 828.928(2)	87 057.485(3)
33	86 826.929(2)	87 062.425(3)
34	86 824.984(3)	87 067.412(3)
35	86 823.078(3)	87 072.399(4)
36	86 821.227(3)	87 077.436(4)
37	86 819.385(4)	87 082.517(5)
38	86 817.602(4)	87 087.625(5)
39	86 815.872(5)	87 092.760(6)
40	86 814.178(5)	87 097.933(7)
41	86 812.520(6)	87 103.116(9)
42	86 810.911(7)	87 108.36(1)
43	86 809.321(9)	87 113.63(1)
44	86 807.80(1)	87 118.92(1)
45	86 806.32(1)	87 124.27(2)
46	86 804.87(1)	87 129.58(2)
47	86 803.49(2)	87 134.94(3)
48	86 802.08(2)	87 140.37(3)
49	86 800.73(3)	87 145.74(4)
50	86 799.47(3)	–
51	86 798.15(4)	–

[a]In units of cm^{-1} and with 1σ statistical uncertainties given in parentheses in units of the least-significant digit. The total uncertainty is the sum in quadrature of these and a 0.01 cm^{-1} systematic uncertainty.

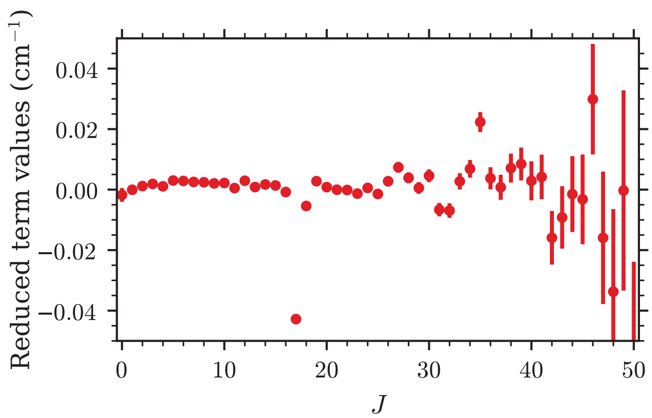

Figure 6. Experimental term values of the $^{13}C^{18}O$ B($v = 0$) level after subtraction by a best-fitting second-order polynomial in terms of $J(J+1)$. The error bars indicate 1σ statistical fitting uncertainties and term-value deviations at some values of J exceeding these uncertainties are indicative of perturbations.

configurations involved: the Π states have a singly occupied (less than half full) π^* orbital and the Σ and Δ states have a π^3 (more than half filled) π orbital. This means that the two kinds of interaction matrix elements will always have opposite signs for the states of interest in CO.

We find anomalously small values for the $\eta_{a(11)\sim a'(9)} = 3.450(61)$ cm^{-1} and $\xi_{a(11)\sim a'(9)} = -0.0018(10)$ cm^{-1} perturbation parameters (listed in Table 10) relative to mass-scaling predictions, yielding 13.195 and -0.035 cm^{-1}, respectively, as well as a surprisingly large magnitude $\eta_{a(11)\sim d(4)} = -34.503(24)$ cm^{-1} value in comparison with the mass-scaling value, -25.770 cm^{-1}. The vibrational overlap integrals between the a($v = 11$) and d($v = 4$) triplet states can be locally and sensitively affected by a node near the internuclear distance of the crossing between the potential energy curves of the two interacting electronic states, and the interaction parameter deviations are probably related to an imperfect knowledge of the $a^3\Pi$ potential energy curve employed in the mass-scaling calculations, which is not well characterised above $v = 6$ [52]. However, no similar problem is observed for any of the other isotopologues and its resolution must await clarification by obtaining spectra of the $a^3\Pi$ state at higher v.

Some perturbation mechanisms in addition to spin–orbit interactions (η) and L-uncoupling (ξ) were examined but their inclusion in the fit model was found to be statistically unjustified given the accuracy of our experimental rovibronic data. Specifically, a second-order spin–spin contribution ($\epsilon_{\Pi\Sigma}$) to the $\Omega = 0$ Λ-doubling of $^3\Pi$ states (mediated via Σ^+ and Σ^- states) as well as a second-order $\mathbf{H}^{\mathbf{SO}} \times \mathbf{H}^{\mathbf{ROT}}$ interaction term (p_3) [54–56] were considered.

The direct or indirect influence upon A($v = 0$) of six levels additional to those listed in Table 10 was tested and ruled out. These higher- and lower-v vibrational levels of the various electronic states in Table 10 were found to have either no measurable impact on A($v = 0$) when included in our model along with estimated interaction parameters, or were highly correlated with molecular constants and/or stronger perturbing effects

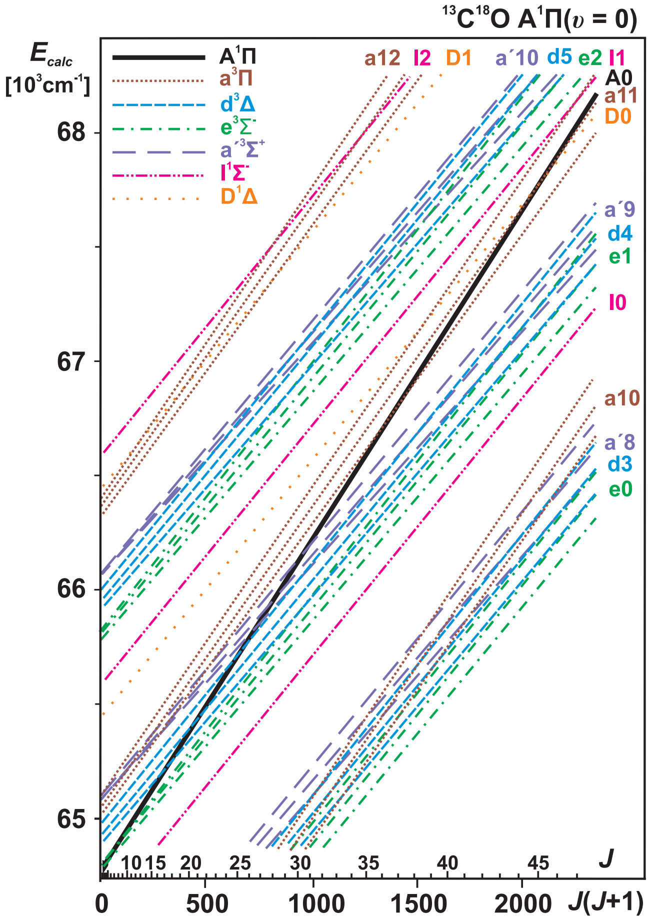

Figure 7. Level diagram for the $^{13}C^{18}O$ A$^1\Pi(v=0)$ state and its neighbourhood in the region of 65,000–68,000 cm^{-1}. The labels denote the electronic state, and to their right the vibrational quantum number. The levels were obtained from the mass-scaled equilibrium molecular constants calculated on the basis of Refs. [14,36] for A$^1\Pi$, Refs. [50,51] for D$^1\Delta$, Refs. [48,52] for a$^3\Pi$, as well as Refs. [48,51] for the a$'^3\Sigma^+$, I$^1\Sigma^-$, d$^3\Delta$ and e$^3\Sigma^-$ states. The $^{13}C^{18}O$ X$^1\Sigma^+$ $G(0)$ value was taken from Ref. [43] to obtain $T_{v=0}$ term.

already included. Details of all the 87 tested interactions are gathered in Supplementary Table 16. We believe that the present deperturbation treatment for the A($v = 0$) state is now limited only by the accuracy and extent of the fitted data set. Perhaps adding more levels and interactions independently quantified with the aid of further spectroscopic measurements would likely expose sensitivity to still-more-remote levels, and it may be that the limits of a reasonable semi-empirical deperturbation treatment has been reached with this analysis. An existing effective Hamiltonian model of the B$^3\Sigma_u^+$ and B$''^3\Pi_u$ states of S_2 [57] is more far-reaching in terms of its energy range than what is done here but this system consists of only two electronic states and exhibits many level crossings.

The Λ-doubling constant of the A$^1\Pi(v=0)$ level generally has a small value for the CO isotopologues. The presently determined value of $q = 2.53(18) \times 10^{-5}$ cm^{-1} has the opposite sign to a value predicted from mass-scaling of the main isotopologue: $q = -1.19 \times 10^{-5}$ cm^{-1}. This Λ-doubling is, in effect, the result of interactions between many levels in the molecule and its modelled value depends sensitively on which levels are excluded from the effective Hamiltonian matrix. The splitting of e- and f-parity levels in a $^1\Pi$ state is the result of interactions with states of Σ symmetry. The number of Σ states explicitly included in the present analysis has increased from our previous work, and a poor extrapolation of the q-parameter is then unsurprising.

Rotational level mixing coefficients and intensity borrowing was also computed using the PGOPHER programme for the model A$^1\Pi$ − X$^1\Sigma^+(0,0)$ transitions and its associated extra lines. Only the unperturbed A−X(0, 0) transition has a nonzero transition dipole moment and any reduction in its perturbed line strengths is proportional to the fractional admixture of other states into the A($v = 0$) level.

Computed and measured oscillator strengths of the A$^1\Pi$ − X$^1\Sigma^+(0,0)$ and forbidden transition Q-branches are plotted in Figure 9 and show generally good agreement. All of the Q-branch transitions in Figure 9 terminate on excited f-parity levels. A qualitatively similar picture and the same level of agreement between modelled and experimental oscillator strengths is found for P- and R-branch transitions that terminate on e-parity levels. These strengths have been reduced by factoring out rotational linestrengths for a pure $^1\Pi - {}^1\Sigma$ transition, and large dips in A−X(0, 0) strengths near $J = 6$, 21 and 27 are the result of level crossings and increased admixture of the e$^3\Sigma^-(v = 1)$, and d$^3\Delta(v = 4)$ F_2 and F_3 states, respectively. Good agreement is found for the oscillator strengths in the a$'^3\Sigma^+$ − X$^1\Sigma^+(11,0)$, d$^3\Delta$ − X$^1\Sigma^+(4,0)$ and e$^3\Sigma^-$ − X$^1\Sigma^+(1,0)$ bands. A significant disagreement between modelled and measured strengths occurs for the Q_{11fe} branch of a$'^3\Sigma^+$ − X$^1\Sigma^+(9,0)$, where the calculated line strengths are significantly larger than observed for $J \gtrsim 5$, while the correct strength is found for the $Q_{11fe}(26)$ line that is most strongly mixed with the A−X(0, 0) $Q(26)$ transition. This suggests that the direct spin–orbit interaction of A($v=0$) and a$'(v = 9)$ is correctly modelled but that indirect mixing via the a($v = 11$) intermediary is not completely reproduced in the analysis. Alternatively, interactions with states not included in the effective Hamiltonian may be involved, or further intensity borrowing from A−X(1, 0).

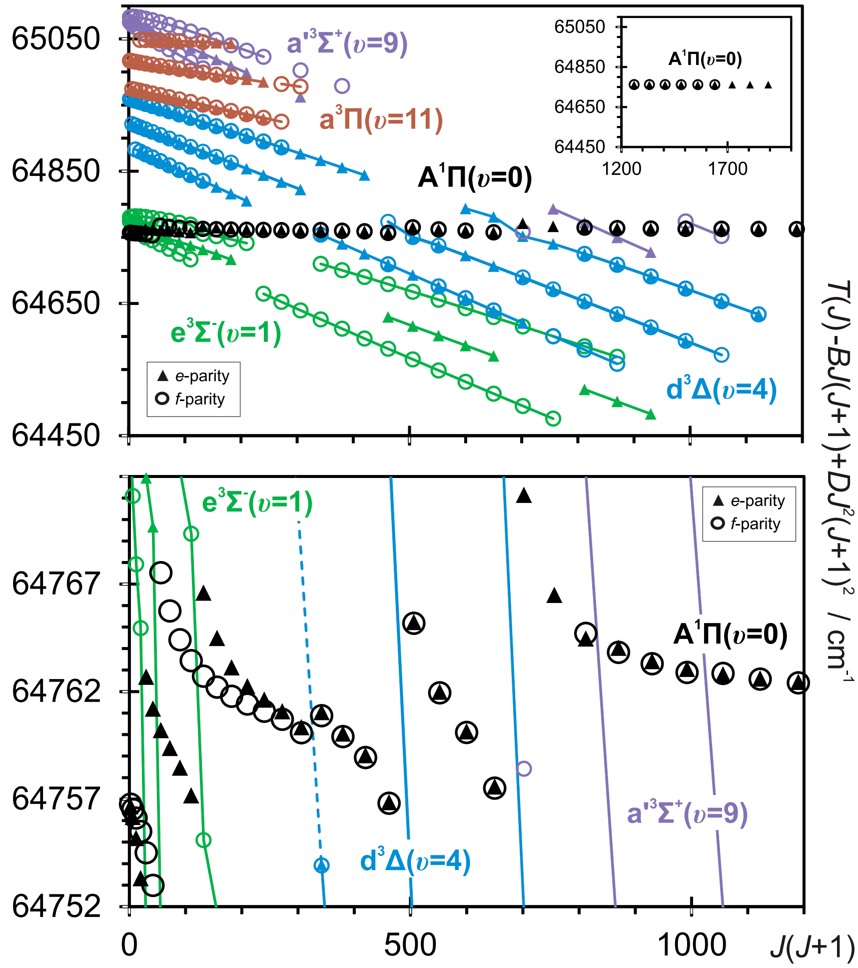

Figure 8. Experimental reduced terms of the $^{13}C^{18}O$ $A^1\Pi(v=0)$ level and its perturbers. The energies are calculated as $T(J) - BJ(J+1) + DJ^2(J+1)^2$ for $B = 1.457$ cm^{-1} and $D = 6.083 \times 10^{-6}$ cm^{-1}.

Table 10. Deperturbed molecular parameters for the $A^1\Pi(v=0)$ level and its direct and indirect perturbers in $^{13}C^{18}O$ as well as for the $B^1\Sigma^+(v=0)$ level.[a,b] Perturbation parameters as discussed in this work and in Refs. [14,17,47].

Constant	$A^1\Pi(v=0)$	$B^1\Sigma^+(v=0)$	$I^1\Sigma^-(v=0)$	$I^1\Sigma^-(v=1)$
T_v	64 762.750 18(60) 64 763.084[c] 64 777.936[d]	86 917.360 32(86) 86 916.702[g]	64571.871[c]	65593.173[c]
B	1.457 416 5(41) 1.457 4(3)[e] 1.457 46[c] 1.32[d]	1.769 764 5(30) 1.769 689(76)[h] 1.769 653(48)[i] 1.769 77(6)[j] 1.769 7(1)[e]	1.145 43[c]	1.130 21[c]
$D \times 10^6$	6.083 0(28) 5.697[c] −194.20[d]	5.538 7(15) 5.524(89)[h] 5.49(34)[i] 6.1(1)[j] 5.8(2)[e]	5.65[l]	5.67[l]
$H \times 10^{12}$	−12.8[f]		2.25[l]	2.25[l]
$q \times 10^5$	2.53(18) −1.19[f]			
$\xi(\sim A, v=0)$			−0.032[m]	0.057[m]
$\eta(\sim a, v=11)$				−2.409[n]
Constant	$D^1\Delta(v=0)$	$e^3\Sigma^-(v=0)$	$e^3\Sigma^-(v=1)$	$e^3\Sigma^-(v=2)$
T_v	65448.421[k]	63 729.173[c]	64 774.962 71(54)	65 802.444[c]
B	1.1339[k]	1.158 49[c]	1.142 611(12)	1.127 38[c]
$D \times 10^6$	5.81[k]	5.67[c]	5.571(18)	5.58[c]
$H \times 10^{12}$	−0.22[l]	−1.50[l]	−1.50[l]	−1.50[l]

(continued).

Table 10. Continued.

Constant	$D^1\Delta(v=0)$	$e^3\Sigma^-(v=0)$	$e^3\Sigma^-(v=1)$	$e^3\Sigma^-(v=2)$
λ		0.52^c	0.536 3(15)	0.54^c
$\gamma \times 10^3$			−2.401(88)	
$\eta(\sim A, v=0)$		-8.480^m	14.400 1(13)	-17.544^m
			14.143^m	
$\xi(\sim A, v=0)$	0.019^m			
$\eta(\sim a, v=11)$	-0.339^n		$2.516^{n,o}$	
$\xi(\sim a, v=11)$			-0.056^n	

Constant	$d^3\Delta(v=3)$	$d^3\Delta(v=4)$	$d^3\Delta(v=5)$	$a'^3\Sigma^+(v=8)$
T_v	$63\,886.481^c$	64 928.697 25(84)	$65\,953.987^c$	$64\,073.372^c$
B	$1.138\,29^c$	1.122937(10)	$1.108\,73^c$	$1.093\,86^c$
$D \times 10^6$	5.361^c	5.153(12)	5.327^c	5.19^c
$H \times 10^{12}$	-0.60^l	-0.60^l	-0.60^l	-0.30^l
A	-15.649^c	−16.581 7(19)	-15.909^c	
$A_D \times 10^4$	-0.92^r	-0.92^r	-0.92^r	
λ	0.67^c	1.124 2(23)	0.85^c	-1.11^c
$\gamma \times 10^3$	-4.95^c	−4.35(18)	-6.28^c	-5.43^c
$\eta(\sim A, v=0)$	27.748(42)	−22.133 6(39)	19.764^m	-4.036^m
	25.7037^m	-23.391^m		
$\eta(\sim a, v=10)^o$		-32.405^n		
$\xi(\sim a, v=10)$		0.073^n		
$\eta(\sim a, v=11)^o$		−34.503(24)	-33.533^n	-16.5999^n
		-25.770^n		
$\xi(\sim a, v=11)$		0.0598(17)	0.074^n	0.039^n
		0.054^n		
$\epsilon(\sim a', v=9)^p$		0.196(37)		

Constant	$a'^3\Sigma^+(v=9)$	$a'^3\Sigma^+(v=10)$	$a^3\Pi(v=10)$	$a^3\Pi(v=11)$
T_v	65 078.497 5(41)	$66\,066.949^c$	$63\,642.313^c$	65 012.3093(45)
B	1.079 761(32)	$1.065\,57^c$	$1.358\,99^c$	1.341 838(54)
$D \times 10^6$	5.188(34)	5.17^c	5.59^c	5.51(17)
$H \times 10^{12}$	-0.30^l	-0.30^l		
A			37.50^c	39.280 9(55)
$A_D \times 10^4$			-2.29^s	-2.17^s
λ	−1.144 5(44)	-1.09^c	-0.0012^s	−0.0121(36)
$\gamma \times 10^3$	−7.02(25)	-5.14^c	3.71^c	3.53^c
o			0.67^c	0.909 8(33)
$p \times 10^3$			2.91^s	1.43(52)
$q \times 10^5$			3.27^c	3.106^c
$\eta(\sim A, v=0)$	2.739(17)	-1.8865^m		
	2.8137^m			
$\eta(\sim a, v=10)^o$	15.1246^n			
$\xi(\sim a, v=10)$	-0.038^n			
$\eta(\sim a, v=11)^o$	3.450(61)			
	13.195^n			
$\xi(\sim a, v=11)$	−0.0018(10)			
	-0.035^n			

[a] All values are in cm^{-1}.
[b] Molecular constants fitted during the model optimisation have uncertainties indicated in parentheses (1σ, in units of the least significant digit). All other parameters were fixed during the fitting procedure. The $^{13}C^{18}O$ ground state level, $X(v=0)$, was fixed to the following constants determined by Coxon and Hajigeorgiou [43]: $G_v = 1031.055619$, $B_v = 1.746408199$, $D_v = 5.0488146 \times 10^{-6}$, $H_v = 4.35471 \times 10^{-12}$, $L_v = -2.4821 \times 10^{-17}$, $M_v = 2.99 \times 10^{-23}$, $N_v = -4.5 \times 10^{-28}$ and $O_v = -2.2 \times 10^{-33}$, all values in cm^{-1}.
[c] Calculated from Ref. [48] based on mass-scaling, where the diagonal spin–spin constant $\lambda = -1.5 \times C$ and the Λ-doubling constants $o = C^{\delta}$ and $q = 2 \times B_{0^+}$. The $^{13}C^{18}O$ $X^1\Sigma^+$ $G(0)$ value was taken from [43] to obtain the $T_{v=0}$ term.
[d] After Ref. [24].
[e] After Ref. [49].
[f] Calculated from Refs. [14,36] based on mass-scaling.
[g] On the basis of the isotopically recalculated values given by Refs.[16,29] for the $B^1\Sigma^+$ as well as using constants determined by Ref. [43] for the $X^1\Sigma^+$ state.
[h] After Ref. [22].
[i] After Ref. [21].
[j] After Ref. [18].
[k] Calculated from Ref. [50] based on mass-scaling.
[l] Calculated from Ref. [51] based on mass-scaling.
[m] The theoretical spin–orbit η and rotational-electronic ξ interaction parameter values were calculated on the basis of the $\mathbf{a}_{A\sim}$ and $\mathbf{b}_{A\sim}$ isotopically invariant given by Hakalla et al. [16] and the appropriate vibrational overlap integrals for $^{13}C^{18}O$ (see text for details).
[n] The value was deduced using elements of an effective Hamiltonian matrix by Field et al. [11] (Table IV) and electronic perturbation matrix elements by Ref. [12] (Table IV) and compare them with the symmetrized matrix elements implemented in the current fit [42] (see text for details).
[o] Determined on the assumption that $\xi \ll \eta$, which condition is very well fulfilled in the present case.
[p] The spin–spin off-diagonal interaction.
[r] Calculated from Ref. [48] based on mass-scaling, where $A_D = 2 \times A_J$ [25].
[s] Obtained and isotopically recalculated from Ref. [52], where the diagonal spin–spin constant $\lambda = 1.5 \times \varepsilon$ and the Λ-doubling constant $p = 2 \times p_+$.

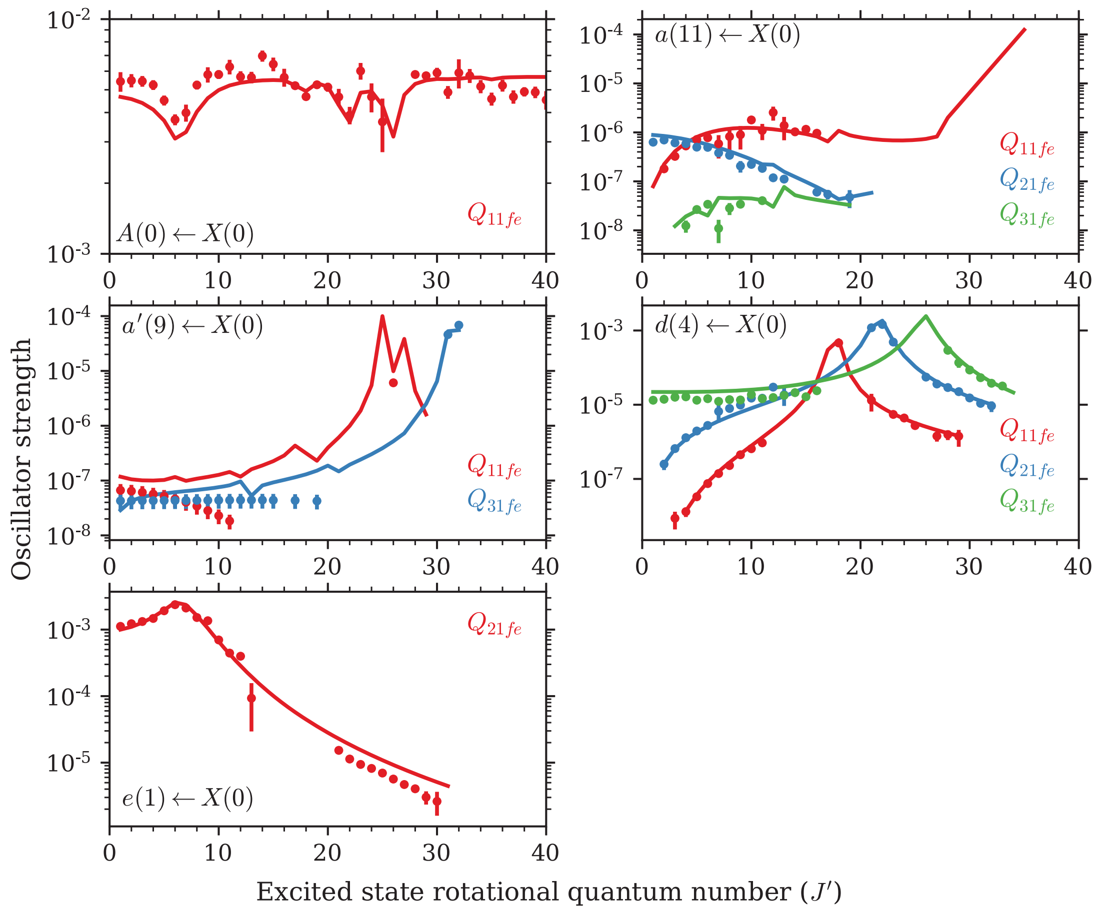

Figure 9. Measured absorption oscillator strengths for Q-branch transitions (points and 1 error bars indicating random fitting uncertainties) and strengths computed from the effective Hamiltonian model (lines). The model strengths were scaled to match the experimental $A(v=0) - X(v=0)$ data and all plotted data are subjected to a common 30% absolute uncertainty.

5. Conclusion

The present study focuses on a comprehensive analysis of spectroscopic data for the $A^1\Pi(v=0)$ state of the $^{13}C^{18}O$ isotopologue of the carbon monoxide molecule. It is a member of a sequence of studies analysing $A^1\Pi(v=0)$ for the isotopologues $^{12}C^{16}O$ [14], $^{13}C^{16}O$ [15], $^{12}C^{18}O$ [17], and $^{13}C^{17}O$ [16]. The complementary properties of various state-of-the-art spectroscopic instruments were exploited for gathering a wealth of accurate information from spectral lines connecting a variety of mutually interacting rovibronic states: the extreme absolute accuracy of a $2+1'$ resonance enhanced two-photon laser ionisation study employing Doppler-free excitation in a molecular beam, the photoemission spectrum from a discharge resolved by FT-VIS spectroscopy and FT-VUV absorption spectroscopy at the SOLEIL synchrotron. All studies were performed at high resolution and special techniques were employed to access high rotational states: notably high temperature and high pressure. The accuracies of measured transition frequencies for the best lines were, respectively, 0.002, 0.003 and 0.02 cm^{-1} in the laser-based, visible FT and synchrotron studies. The level structure of the $A^1\Pi(v=0)$ state of $^{13}C^{18}O$ was targeted via the $A^1\Pi - X^1\Sigma^+(0,0)$ and $B^1\Sigma^+ - A^1\Pi(0,0)$ bands, while information was also gathered on the direct and indirect perturber states $e^3\Sigma^-(v=0,1,2)$, $d^3\Delta(v=3,4,5)$, $a'^3\Sigma^+(v=8,9,10)$, $D^1\Delta(v=0)$, $I^1\Sigma^-(v=0,1)$ and $a^3\Pi(v=10,11)$. The $B^1\Sigma^+ - X^1\Sigma^+(0,0)$ band was investigated by FT-VUV spectroscopy to connect the visible emission study on an absolute energy scale with respect to the ground state. Weak perturbations in the $B^1\Sigma^+(v=0)$ level were observed and included in the analysis.

A comprehensive set of deperturbed constants and level energies for the $A(v=0)$ state and its perturbers is determined from this set of combined data. The complexity of the present deperturbation analysis exceeds that of the previous studies on other isotopologues and is made possible here by a more extensive highly accurate data set. The number of modelled perturber states is extended and we determine molecular constants for some triplet levels that do not exhibit a crossing with $A^1\Pi(v=0)$. In general, up to 87 vibronic interactions are considered between $A(v=0)$, $A(v=1)$, $I(v=0,1,2)$ and $D(v=0,1,2)$ singlet states and a large set of the $a(v=10,11,12)$, $d(v=3,4,5,6)$, $a'(v=8,9,10,11)$ and $e(v=0,1,2,3,4)$ triplet levels. Some mutual interactions of various triplet states perturbing the $A(v=0)$ level are determined in the analysis which had not been distinguishable in our previous studies focusing on other isotopologues. Although eight lines of the vast body of observed transitions could not be identified, there is no need to invoke additional band systems beyond those well known to CO to describe the observed spectroscopic patterns, as was done in Ref. [24].

The present study surpasses in complexity any previous similar analyses of the CO molecule, which is a prototypical species for perturbations. There are 15 mutually interacting electronic-vibrational levels included to reproduce over 900 line frequencies to a high level of accuracy. The deperturbation model also reproduces the borrowing of absorption oscillator strength by the observed forbidden bands from the main transition $A^1\Pi - X^1\Sigma^+(0,0)$.

Acknowledgements

The authors are grateful to the general and technical staff of SOLEIL for providing beam time under projects no. 20120653 and no. 20160118.

Disclosure statement

No potential conflict of interest was reported by the authors.

Funding

RH thanks LASERLAB-EUROPE for support of this research (Grants EUH2020-RIP-654148 and EC's- SPF-284464) as well as European Regional Development Fund and the Polish state budget within the framework of the Carpathian Regional Operational Programme (RPPK.01.03.00-18-001/10) through the funding of the Center for Innovation and Transfer of Natural Science and Engineering Knowledge of the University of Rzeszów. AH acknowledges support from the Postdoctoral Fellowship program of PSL Research University Paris and NASA Postdoctoral Program. WU acknowledges financial support from the European Research Council (ERC) under the European Union's Horizon 2020 research and innovation programme (Grant Agreement No. 670168). RWF is grateful to the US National Science Foundation (Grant CHE-1361865).

References

[1] Y. Sheffer, M. Rogers, S.R. Federman, D.L. Lambert, and R. Gredel, Astrophys. J. **667** (2), 1002 (2007).
[2] S. Perez, S. Casassus, F. Ménard, P. Roman, G. Van Der Plas, L. Cieza, C. Pinte, V. Christiaens, and A.S. Hales, Astrophys. J. **798** (2), 85 (2015).
[3] K. Heng and J.R. Lyons, Astrophys. J. **817**, 149 (2016).
[4] P. Noterdaeme, J.-K. Krogager, S. Balashev, J. Ge, N. Gupta, T. Krühler, C. Ledoux, M.T. Murphy, I. Pâris, P. Petitjean, H. Rahmani, R. Srianand, and W. Ubachs, Astron. Astroph. **597**, A82 (2017).
[5] M. Daprà, M.L. Niu, E.J. Salumbides, M.T. Murphy, and W. Ubachs, Astroph. J. **826** (2), 192 (2016).
[6] M. Daprà, P. Noterdaeme, M. Vonk, M.T. Murphy, and W. Ubachs, Mon. Not. Roy. Astron. Soc. **467** (4), 3848 (2017).
[7] M. Eidelsberg and F. Rostas, Astron. Astroph. **235** (1–2), 472 (1990).
[8] M. Eidelsberg, Y. Viala, F. Rostas, and J.J. Benayoun, Astron. Astrophys. Suppl. Ser. **90**, 231 (1991).
[9] P. Cacciani, W. Ubachs, P.C. Hinnen, C. Lyngå, A. L'Huillier, and C.-G. Wahlström, Astroph. J. Lett. **499** (2), L223 (1998).
[10] W. Ubachs, I. Velchev, and P. Cacciani, J. Chem. Phys. **113** (2), 547 (2000).
[11] R.W. Field, S.G. Tilford, R.A. Howard, and J.D. Simmons, J. Mol. Spectr. **44** (2), 347 (1972).
[12] R.W. Field, B.G. Wicke, J.D. Simmons, and S.G. Tilford, J. Mol. Spectr. **44** (2), 383 (1972).
[13] E.J. Salumbides, M.L. Niu, J. Bagdonaite, N. de Oliveira, D. Joyeux, L. Nahon, and W. Ubachs, Phys. Rev. A **86**, 022510 (2012).
[14] M.L. Niu, E.J. Salumbides, D. Zhao, N. de Oliveira, D. Joyeux, L. Nahon, R.W. Field, and W. Ubachs, Mol. Phys. **111**, 2163 (2013).
[15] M.L. Niu, R. Hakalla, T.M. Trivikram, A.N. Heays, N. de Oliveira, E.J. Salumbides, and W. Ubachs, Mol. Phys. **114** (19), 2857 (2016).
[16] R. Hakalla, M.L. Niu, R.W. Field, A.N. Heays, E.J. Salumbides, G. Stark, J.R. Lyons, M. Eidelsberg, J.L. Lemaire, S.R. Federman, N. de Oliveira, and W. Ubachs, J. Quant. Spectr. Rad. Transfer **189**, 312 (2017).
[17] T.M. Trivikram, R. Hakalla, A.N. Heays, M.L. Niu, S. Scheidegger, E.J. Salumbides, N. de Oliveira, R.W. Field, and W. Ubachs, Mol. Phys. **115** (24), 3178 (2017).
[18] C. Haridass, S.P. Reddy, and A.C. Le Floch, J. Mol. Spectr. **168** (2), 429 (1994).
[19] C. Haridass, S.P. Reddy, and A.C. Le Floch, J. Mol. Spectr. **167** (2), 334 (1994).
[20] C.V.V. Prasad, G.L. Bhale, and S.P. Reddy, J. Mol. Spectr. **104**, 165 (1984).
[21] Z. Malak, M. Rytel, J.D. Janjić, and D.S. Pešić, Acta Phys. Hung. **55** (1–4), 85 (1984).
[22] R. Kępa, Can. J. Phys. **66** (11), 1012 (1988).
[23] R. Kępa, M. Ostrowska-Kopeć, I. Piotrowska, M. Zachwieja, R. Hakalla, W. Szajna, and P. Kolek, J. Phys. B **47** (4), 045101 (2014).
[24] J.L. Lemaire, M. Eidelsberg, A.N. Heays, L. Gavilan, S.R. Federman, G. Stark, J.R. Lyons, N. de Oliveira, and D. Joyeux, J. Phys. B **49** (15), 154001 (2016).
[25] A.J. de Nijs, E.J. Salumbides, K.S.E. Eikema, W. Ubachs, and H.L. Bethlem, Phys. Rev. A **84**, 052509 (2011).
[26] W. Ubachs, K.S.E. Eikema, W. Hogervorst, and P.C. Cacciani, J. Opt. Soc. Am. B **14** (10), 2469 (1997).
[27] M.L. Niu, F. Ramirez, E.J. Salumbides, and W. Ubachs, J. Chem. Phys. **142**, 044302 (2015).
[28] S. Xu, R. van Dierendonck, W. Hogervorst, and W. Ubachs, J. Mol. Spectr. **201**, 256 (2000).
[29] R. Hakalla, M. Zachwieja, and W. Szajna, J. Phys. Chem. A **117** (47), 12299 (2013).

[30] R. Hakalla, W. Szajna, and M. Zachwieja, J. Phys. B **45** (21), 215102 (2012).
[31] R. Hakalla, W. Szajna, M. Zachwieja, and R. Kępa, Acta Phys. Pol. A **122**, 674 (2012).
[32] R. Hakalla, Roy. Soc. Chem. Adv. **4**, 44394 (2014).
[33] R. Hakalla, M. Zachwieja, and W. Szajna, J. Quant. Spectr. Rad. Transfer **140**, 7 (2014).
[34] N. de Oliveira, M. Roudjane, D. Joyeux, D. Phalippou, J.-C. Rodier, and L. Nahon, Nat. Photon. **5** (3), 149 (2011).
[35] N. de Oliveira, D. Joyeux, M. Roudjane, J.-F. Gil, B. Pilette, L. Archer, K. Ito, and L. Nahon, J. Synch. Rad. **23** (4), 887 (2016).
[36] M.L. Niu, E.J. Salumbides, A.N. Heays, N. de Oliveira, R.W. Field, and W. Ubachs, Mol. Phys. **114** (5), 627 (2016).
[37] L. Gavilan, J.L. Lemaire, M. Eidelsberg, S.R. Federman, G. Stark, A.N. Heays, J.-H. Fillion, J.R. Lyons, and N. de Oliveira, J. Phys. Chem. A **117** (39), 9644 (2013).
[38] G. Stark, B.R. Lewis, S.T. Gibson, and J.P. England, Astrophys. J. **505** (1), 452 (1998).
[39] M.L. Niu, A.N. Heays, S. Jones, E.J. Salumbides, E.F. van Dishoeck, N. de Oliveira, L. Nahon, and W. Ubachs, J. Mol. Spectr. **315**, 137 (2015).
[40] S. Xu, G. Sha, B. Jiang, W. Sun, X. Chen, and C. Zhang, J. Chem. Phys. **100** (9), 6122 (1994).
[41] J.W. Brault, Microchimica Acta **93** (1), 215 (1987).
[42] C.M. Western, Pgopher: A Program for Simulating Rotational Structure. Technical Report, University of Bristol, Bristol, 2017.
[43] J.A. Coxon and P.G. Hajigeorgiou, J. Chem. Phys. **121** (7), 2992 (2004).
[44] F. Rostas, M. Eidelsberg, A. Jolly, J.L. Lemaire, A. Le Floch, and J. Rostas, J. Chem. Phys. **112** (10), 4591 (2000).
[45] A. Le Floch, J. Rostas, and F. Rostas, Chem. Phys. **142** (2), 261 (1990).
[46] M. Eidelsberg and F. Rostas, Astroph. J. Suppl. Ser. **145** (1), 89 (2003).
[47] R. Hakalla, M.L. Niu, R.W. Field, E.J. Salumbides, A.N. Heays, G. Stark, J.R. Lyons, M. Eidelsberg, J.L. Lemaire, S.R. Federman, M. Zachwieja, W. Szajna, P. Kolek, I. Piotrowska, M. Ostrowska-Kopeć, R. Kępa, N. de Oliveira, and W. Ubachs, Roy. Soc. Chem. Adv. **6**, 31588 (2016).
[48] R.W. Field, Ph. D. thesis, Harvard University, 1971.
[49] C.V.V. Prasad and S.P. Reddy, J. Mol. Spectr. **130**, 62 (1988).
[50] C. Kittrell and B.A. Garetz, Spectrochim. Acta **45** (1), 31 (1989).
[51] A.C. Le Floch, F. Launay, J. Rostas, R.W. Field, C.M. Brown, and K. Yoshino, J. Mol. Spectr. **121** (2), 337 (1987).
[52] S. Yamamoto and S. Saito, J. Chem. Phys. **89** (4), 1936 (1988).
[53] C.M. Western, J. Quant. Spectr. Rad. Transfer **186**, 221 (2017).
[54] C. Effantin, F. Michaud, F. Roux, J. d'Incan, and J. Verges, J. Mol. Spectr. **92** (2), 349 (1982).
[55] C. Amiot and K. Islami, J. Mol. Spectr. **118** (2), 363 (1986).
[56] A. Wada and H. Kanamori, J. Mol. Spectr. **200** (2), 196 (2000).
[57] M.E. Green and C.M. Western, J. Chem. Phys. **104** (3), 848 (1996).